

# Regional seismic wave propagation ( $Lg$ and $S_n$ ) and $P_n$ attenuation in the Arabian Plate and surrounding regions

Khaled Al-Damegh,<sup>1</sup> Eric Sandvol,<sup>2</sup> Ali Al-Lazki<sup>3</sup> and Muawia Barazangi<sup>1</sup>

<sup>1</sup>Institute for the Study of the Continents and Department of Earth and Atmospheric Sciences, Cornell University, Snee Hall, Ithaca, NY 14853, USA.

E-mail: Barazangi@geology.cornell.edu

<sup>2</sup>Department of Geological Sciences, University of Missouri, 101 Geology Building, Columbia, MO 65211, USA

<sup>3</sup>Department of Earth Sciences, College of Sciences, Sultan Qaboos University, Alkhod, Sultanate of Oman

Accepted 2004 January 12. Received 2003 December 8; in original form 2003 June 25

## SUMMARY

Continuous recordings of 17 broadband and short-period digital seismic stations from a newly established seismological network in Saudi Arabia, along with digital recordings from the broadband stations of the GSN, MEDNET, GEOFON, a temporary array in Saudi Arabia, and temporary short period stations in Oman, were analysed to study the lithospheric structure of the Arabian Plate and surrounding regions. The Arabian Plate is surrounded by a variety of types of plate boundaries: continental collision (Zagros Belt and Bitlis Suture), continental transform (Dead Sea fault system), young seafloor spreading (Red Sea and the Gulf of Aden) and oceanic transform (Owen fracture zone). Also, there are many intraplate Cenozoic processes such as volcanic eruptions, faulting and folding that are taking place.

We used this massive waveform database of more than 6200 regional seismograms to map zones of blockage, inefficient and efficient propagation of the  $Lg$  and  $S_n$  phases in the Middle East and East Africa. We observed  $Lg$  blockage across the Bitlis Suture and the Zagros fold and thrust belt, corresponding to the boundary between the Arabian and Eurasian plates. This is probably due to a major lateral change in the  $Lg$  crustal waveguide. We also observed inefficient  $Lg$  propagation along the Oman mountains. Blockage and inefficient  $S_n$  propagation is observed along and for a considerable distance to the east of the Dead Sea fault system and in the northern portion of the Arabian Plate (south of the Bitlis Suture). These mapped zones of high  $S_n$  attenuation, moreover, closely coincide with extensive Neogene and Quaternary volcanic activity. We have also carefully mapped the boundaries of the  $S_n$  blockage within the Turkish and Iranian plateaus. Furthermore, we observed  $S_n$  blockage across the Owen fracture zone and across some segments of the Red Sea. These regions of high  $S_n$  attenuation most probably have anomalously hot and possibly thin lithospheric mantle (i.e. mantle lid). A surprising result is the efficient propagation of  $S_n$  across a segment of the Red Sea, an indication that active seafloor spreading is not continuous along the axis of the Red Sea. We also investigated the attenuation of  $P_n$  phase ( $Q_{P_n}$ ) for 1–2 Hz along the Red Sea, the Dead Sea fault system, within the Arabian Shield and in the Arabian Platform. Consistent with the  $S_n$  attenuation, we observed low  $Q_{P_n}$  values of 22 and 15 along the western coast of the Arabian Plate and along the Dead Sea fault system, respectively, for a frequency of 1.5 Hz. Higher  $Q_{P_n}$  values of the order of 400 were observed within the Arabian Shield and Platform for the same frequency. Our results based on  $S_n$  and  $P_n$  observations along the western and northern portions of the Arabian Plate imply the presence of a major anomalously hot and thinned lithosphere in these regions that may be caused by the extensive upper mantle anomaly that appears to span most of East Africa and western Arabia.

**Key words:** Arabian Plate,  $Lg$  and  $S_n$  attenuation, Middle East, regional seismic waves, tectonics.

## 1 INTRODUCTION

The Arabian Plate is surrounded by diverse plate boundaries (Fig. 1). To the southwest and south the Arabian Plate is bounded by seafloor spreading along the Red Sea, the Gulf of Aden and the Arabian Sea (McKenzie *et al.* 1970). To the east and north, the Arabian Plate is colliding with the Eurasian Plate along the Zagros and Bitlis sutures (McKenzie 1976). The Dead Sea fault system is located along the northwestern boundary of the plate. The fault is left-lateral with a minor component of rotation that results in the development of pull-apart basins, such as the Dead Sea rift basin (Garfunkel 1981). The interior of the plate is dominated by the late Proterozoic Arabian Shield and the Arabian Phanerozoic Platform. The platform was affected by numerous intraplate tectonism throughout Mesozoic and Cenozoic time, for example the Palmyrides and Euphrates fault system within the northern part of the platform (Brew *et al.* 2001; Hempton 1987).

Though the surface geology of the Arabian Plate and surrounding plate boundaries has been well studied, there are relatively few studies concerning the crustal and upper mantle structure of the Arabian Plate. This study focuses on understanding the propagation characteristics of the regional seismic waves  $P_n$ ,  $P_g$ ,  $S_n$  and  $L_g$ . In particular,  $L_g$  is shown to be sensitive to lateral variations in the crustal thickness as well as the rheology of the crustal rocks.  $S_n$ , however, is very sensitive to lateral variations in the mantle lid and/or to the presence of asthenospheric material very close to or immediately below the crust. Few studies are available in the literature concerning the propagation of  $S_n$  and  $L_g$  in the Middle East (Kadinsky-Cade *et al.* 1981; Rodgers *et al.* 1997; Mellors *et al.* 1999; Gok *et al.* 2000; Sandvol *et al.* 2001). This study, however, makes use of a massive new waveform database produced by the recently established broadband seismic array in Saudi Arabia. This database provided us with the opportunity to extend our study to the whole Arabian Plate and the surrounding regions; i.e. this study is by

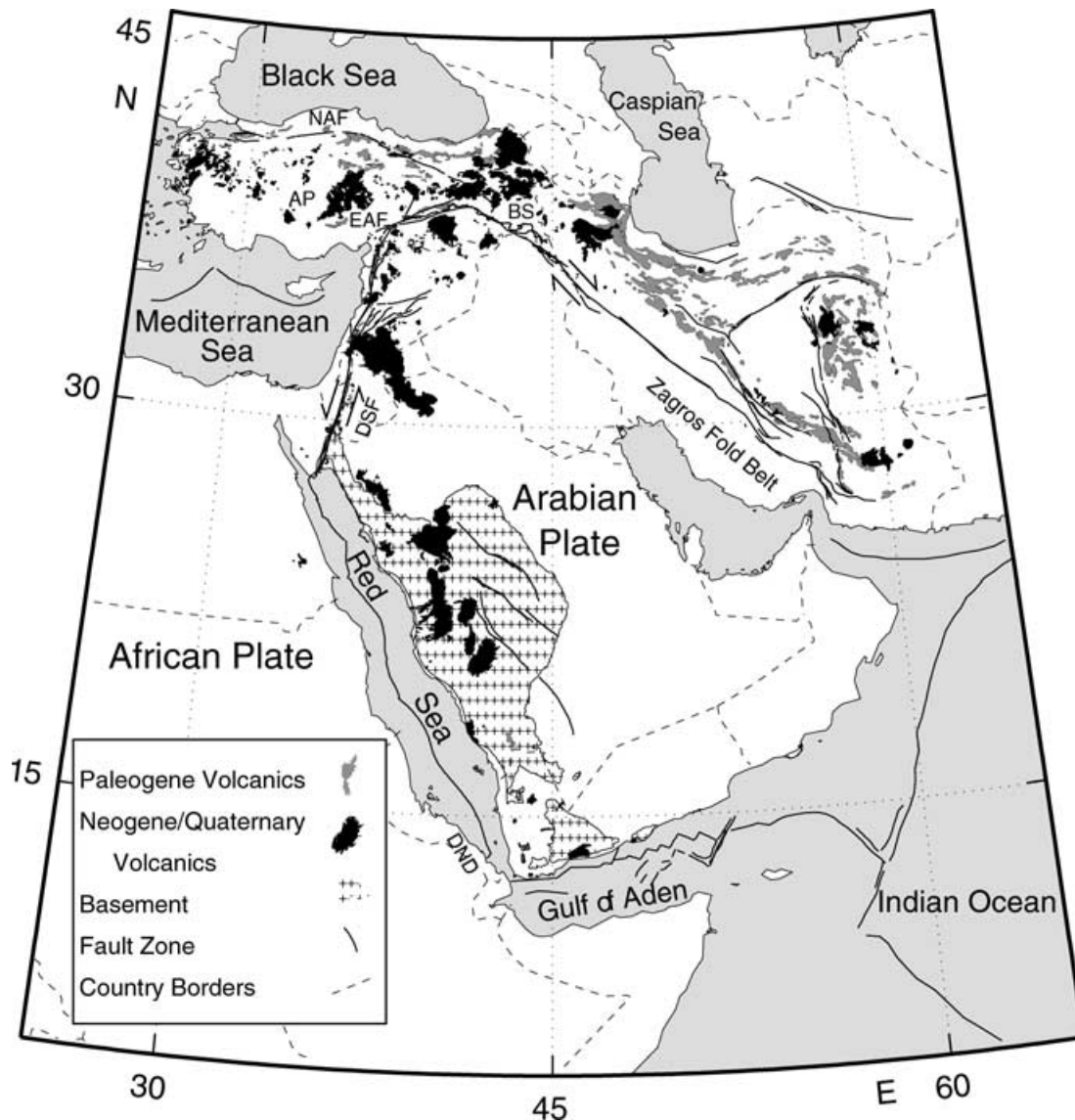


**Figure 1.** A simplified tectonic map showing the main tectonic features of the Arabian Plate and only surrounding regions. AP: Anatolian Plateau; NAF: North Anatolian fault; EAF: East Anatolian fault; BS: Bitlis Suture; DSF: Dead Sea fault; DND: Danakil Depression.

far the most comprehensive and complete that can be accomplished at present.

### 1.1 Tectonic setting

The Arabian Plate consists of a Precambrian shield bounded by a sedimentary platform (see Fig. 1). The eastern part of the shield is overlapped unconformably by Phanerozoic sedimentary layers dipping eastward and reaching over 10 km in thickness (Powers *et al.* 1966; Sandvol *et al.* 1998; Mokhtar *et al.* 2001). The Arabian Shield was part of the Nubian Shield until the Oligocene, during which a rifting process started in Afar and later propagated eastward, creating the Gulf of Aden, and northward, creating the Red Sea (Cochran & Martinez 1988). Assuming purely active rifting, the crust of the Red Sea was thought to be oceanic extending from the shorelines of Africa to Arabia (e.g. McKenzie *et al.* 1970; Le Pichon & Girdler 1988). Assuming purely passive rifting, on the other hand, the Red Sea crust was thought to consist of extended 'transitional' continental crust (Cochran 1983). Neogene and Quaternary volcanics were observed along the western part of the Arabian Plate (Camp & Roobol 1992).

Before the rifting of the Red Sea, the Afro-Arabian and the Eurasian plates were separated by the Neo-Tethys, which was being subducted under the Eurasian Plate (Stocklin 1974). The Arabian Plate collided with the Eurasian Plate in the early Miocene (Dewey *et al.* 1973; Dewey & Sengor 1979). The Bitlis Suture, the Zagros fold and thrust belt, and the East Anatolian left-lateral strike slip fault mark the collision zone (e.g. Sengor & Kidd 1979). North of the Bitlis Suture and east of the Zagros lies the Iranian–Anatolian Plateau. This plateau is a major topographic feature in the region, which was uplifted in Pliocene and characterized by pervasive late Tertiary–Quaternary basalts (Sengor & Kidd 1979). Recent GPS measurements over the Anatolian Block (Barka & Reilinger 1997) show that the block is escaping to the west. Most of the Lesser and Greater Caucasus are believed to have formed within the same time frame as the Arabian–Eurasian collision, during the middle to late Pliocene (e.g. Phillip *et al.* 1989).

The South Caspian Sea is a remnant Palaeo-Tethys lithosphere (Zonenshain & LePichon 1986). The crust of the Gulf of Oman is also believed to be oceanic and being subducted in a northerly direction beneath the Makran region (e.g. Farhoudi & Karig 1977; Jacob & Quittmeyer 1979).

The Mesopotamian Foredeep, which is located to the west of the Zagros fold and thrust belt, consists of thick sediments that increase in thickness eastward (Seber *et al.* 1997). The Dead Sea fault system is a transcontinental boundary between the Arabian and African plates. It is considered a leaky left lateral transform fault with several portions of the fault system producing pull-apart basins such as the Dead Sea Trough and the Gulf of Aqaba (Garfunkel 1981). Garfunkel (1981) suggested that spreading centres located in the middle of the pull-apart basins probably extend into the lithospheric mantle and are indicative of considerable lithospheric thinning.

### 1.2 Regional seismic waves *Pn*, *Pg*, *Sn* and *Lg*

Regional seismic phases have been essential in exploring regional crustal and mantle lid structure and rheology. *Lg* is a crustal guided wave that usually can be found within velocity and frequency windows of 3.1 to 3.6 km s<sup>-1</sup> and 0.5 to 5.0 Hz respectively. The *Lg* phase has been modelled as higher-mode Love and Rayleigh waves and also as a sequence of wide-angle multiply reflected *S* waves trapped in the crustal waveguide (Bouchon 1982; Kennett 1986; Bostock & Kennett 1990). Observations of *Lg* propagation have

demonstrated that *Lg* is blocked for paths in oceanic or very thin continental crust (Press & Ewing 1952; Searle 1975; Zhang & Lay 1995). Observational as well as theoretical studies indicate that the crustal waveguide plays a primary role in *Lg* propagation characteristics (Kennett 1986; Bostock & Kennett 1990; Baumgardt & Der 1997; Rodgers *et al.* 1997); rapid changes in the crustal thickness block or weaken *Lg* propagation (Bostock & Kennett 1990; Fan & Lay 1998; Mitchell *et al.* 1997); and *Lg* propagation can be severely weakened by deep sedimentary basins and intrinsic attenuation (e.g. Nuttli 1980; Baumgardt & Der 1997). Recent *Lg* propagation studies utilize the *Lg/Pg* ratio to reflect changes in the ray path (e.g. Baumgardt 1996; Fan & Lay 1998; Hartse *et al.* 1998; Sandvol *et al.* 2001). Unlike the *Lg* phase, the *Pg* phase is reasonably insensitive to crustal structure. Consisting of direct *P*-wave energy from crustal earthquakes, the *Pg* seismic phase is usually found in a velocity window between 5.0 and 6.5 km s<sup>-1</sup>.

The *Sn* phase is a high-frequency guided seismic wave that travels in the lithospheric mantle with a typical frequency of 1 to 4 Hz or more. The typical velocity for *Sn* is around 4.7 km s<sup>-1</sup> in stable continental and oceanic lithosphere and less than that in more tectonically active regions (Huestis *et al.* 1973; Kadinsky-Cade *et al.* 1981). The *Sn* wave train can last up to 2 min and has been recorded for distances up to 35° (e.g. Molnar & Oliver 1969; Huestis *et al.* 1973). The first prominent phase on the seismic record for regional distances is *Pn*, a mantle lid guided wave with a velocity window of 7.8 to 8.1 km s<sup>-1</sup>.

Previous studies of regional waves in the Middle East have found a number of important regions with anomalous propagation characteristics. Kadinsky-Cade & Barazagni (1982) found a zone of *Lg* blockage across the Zagros fold and thrust belt as well as a continuous zone of *Sn* attenuation extending from the northern Iranian Plateau to central and western Turkey. Using more data from several broadband stations and the Iranian long period array (ILPA), Rodgers *et al.* (1997) extended these zones of *Sn* and *Lg* attenuation. They also found good correlation between *Sn* attenuating zones and the low *Pn* velocities published by Hearn & Ni (1994). An *Sn* and *Lg* tomography study by Sandvol *et al.* (2001) indicated that the South Caspian Sea crust is an oceanic lithosphere. In addition, that study outlined the main tectonic features such as the Zagros and Bitlis sutures, the Arabian Shield, the Arabian Platform, the Dead Sea fault system and areas correlated with Neogene/Quaternary volcanics.

## 2 SEISMIC DATA

The data set used for this study is by far the most recent and complete one. This study integrated new data from more than six different networks, temporary stations and a global permanent station (see Fig. 2a). The main part of the data set came from the Saudi National Seismic Network (SNSN), which consists of 13 broadband stations and four short-period one-component stations. Data from four temporary short-period three-component stations in Oman and data from RAYN, an IRIS broadband permanent station, were also used. Data from two GEOSCOPE stations (ATD and AAE in Djibouti and Addis Ababa respectively) were requested through IRIS and used in this study. In total more than 15 000 regional seismograms were checked for quality of signal-to-noise and electronic noise. Seismograms with low signal-to-noise ratio or electronic noise that cannot be removed were discarded. Only regional earthquakes with distances between 175 and 2000 km were used (see Fig. 2b). Earthquakes with a depth of more than 35 km were not used for the *Lg/Pg* analysis. In total about 2400 seismograms were found to be suitable

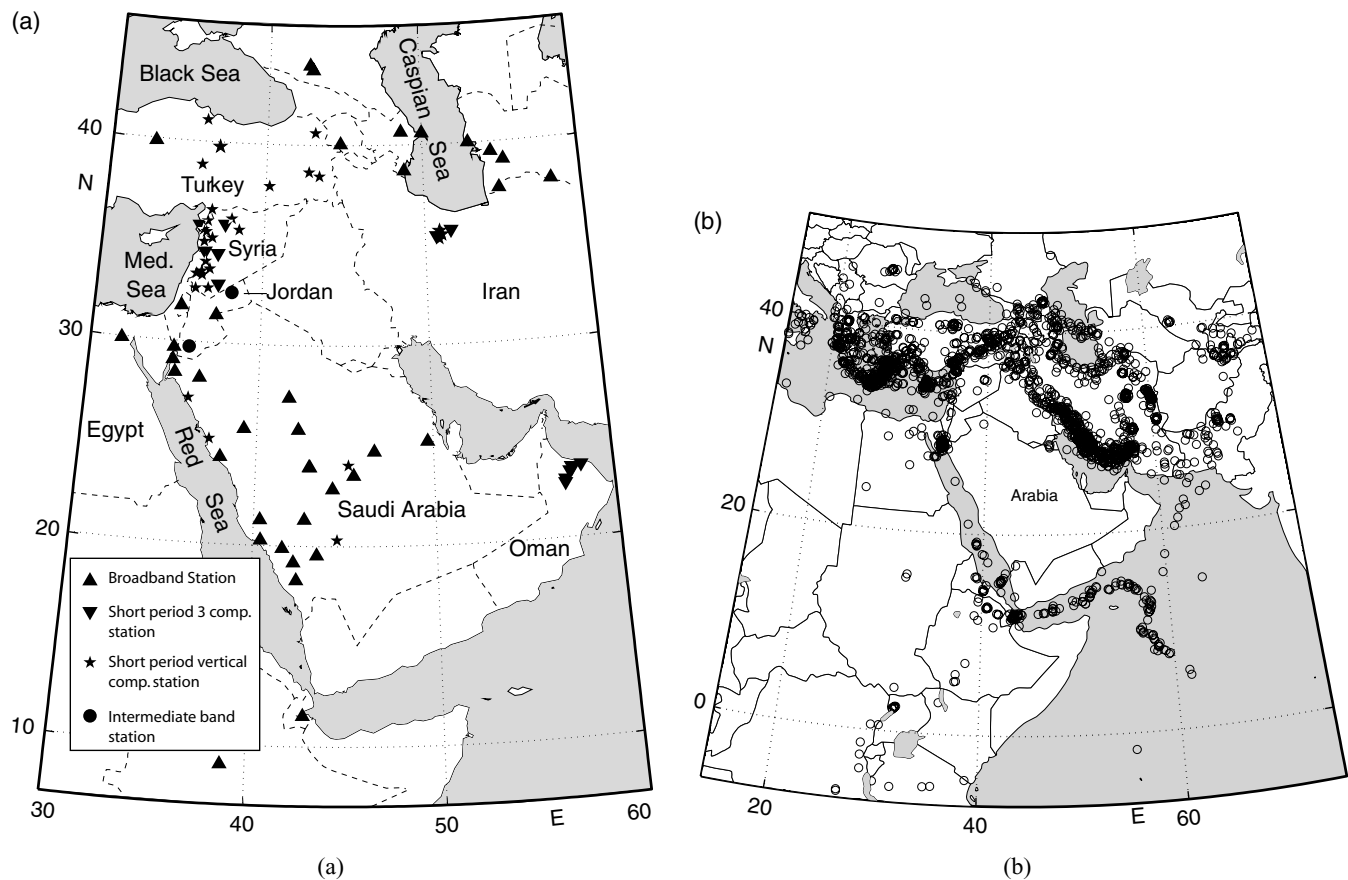


Figure 2. Maps showing the seismic stations (a) and earthquakes (b) used in this study.

for this study and were combined with the archived regional data set from the Cornell Middle East Project database.

### 3 QUALITATIVE EFFICIENCIES AND WAVEFORM EXAMPLES

For *Lg* observations, only seismograms with a clear *Pg* phase arrival were used. *Lg* observations were classified according to the amplitude of the *Lg* phase relative to the *Pg* phase. When the *Lg* amplitude was approximately twice the *Pg* amplitude, the seismogram was classified as efficient. Seismograms were classified as inefficient when the relative amplitudes were approximately equal. In the case of *Lg* amplitudes smaller than *Pg* amplitudes, seismograms were classified as blocked or absent. Clearly the above criteria are qualitative in nature, and for most ray paths considered in this study the details of the propagation of *Pg* do not significantly affect our observations. To avoid errors in timing and event mislocation, *Lg* and *Pg* windows were determined according to the picked first arrival. Crustal thickness and velocity do not influence this procedure. Fig. 3 is a ray map showing the classified *Lg* ray paths for all the data used in this study.

The *Sn* observations were classified into three groups: (1) efficient, (2) inefficient and (3) blocked. We classified *Sn*, which arrives within a velocity window of 4.3–4.7 km s<sup>-1</sup>, as efficient if it contained a high-frequency (>2 Hz) wave train and the average *Sn* amplitude is twice that of the average noise prior to the first arrival. An inefficient *Sn* lacks one or more features of efficient *Sn*. When no *Sn* signal is observed, the seismogram is classified as blocked. Fig. 4 shows all the classified *Sn* ray paths for all the data used in

this study. We also show Figs 3 and 4 in more detail as an electronic supplemental figures (supplemental Figs S1 and S2).

Different filters were used to identify *Sn*, *Lg* and *Pg* phases. Crustal velocities of 5.2–6.2 km s<sup>-1</sup> for *Pg*, 4.1–4.6 km s<sup>-1</sup> for *Sn* and 3.1–3.6 km s<sup>-1</sup> for *Lg* were assumed. Windows for *Pg*, *Sn* and *Lg* were determined based on first arrival picking and a crustal thickness of 35 km.

#### 3.1 *Lg* observations

Our *Lg* efficiency ray map is shown in Fig. 3 and some examples from our data set are shown in Figs 5 and 6. In our *Lg* ray map the Arabian Plate is mostly well covered by *Lg* ray paths, except in the southeastern part. In general the *Lg* observations shown in Fig. 3 are consistent, where most regions can be classified as regions of blockage, inefficient or efficient. For example, paths from earthquakes in the Zagros to stations in Saudi Arabia and Jordan show efficient *Lg* (Figs 6b-1, 2, 4 and 5). However, stations in Oman recorded inefficient *Lg* (Figs 6c-2 and 5). For earthquakes east of the Zagros to the same regions, *Lg* becomes mostly blocked or inefficient (Figs 6b-3 and 6, Figs 6c-3). *Lg* was mostly blocked (Figs 6a-5 and 6) for paths in the Mediterranean Sea. We observed very few earthquakes along and west of the Red Sea. Interestingly, for most of these events *Lg* was efficient and occasionally inefficient or blocked (Figs 5b-1, 2 and 3). Earthquakes along the Gulf of Aden show efficient *Lg* propagation along the Arabian Plate (Figs 5c-1, and 2). *Lg* was blocked for earthquakes along the Owen fracture zone. Few ray paths were observed in the African Plate and were recorded at stations KEG, AAE and ATD. The paths corresponding

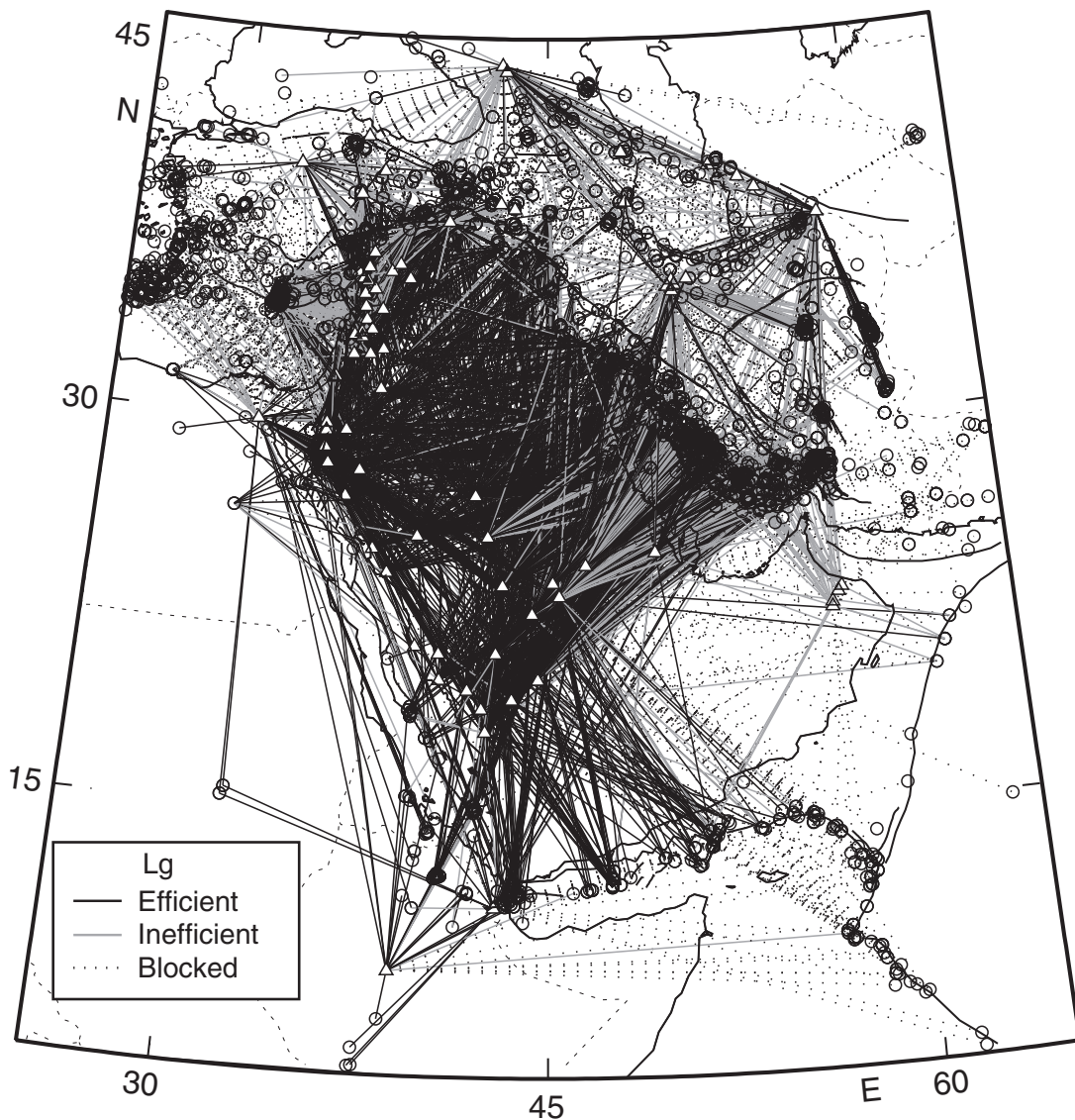


**Figure 3.** Map showing more than 6200 *Lg* ray path efficiencies. Each ray path corresponds to an earthquake–station pair. The seismograms corresponding to these rays were classified by visible inspection by the authors as efficient, inefficient or blocked. The Arabian Plate is well covered by mostly efficient *Lg* ray paths. Ray paths from Zagros to Oman stations are mostly inefficient. Less ray path coverage is available across the Red Sea and Afar. Efficient as well as blocked and inefficient *Lg* ray paths were observed in the Red Sea region.

to these events show efficient *Lg* propagation (e.g. Fig. 5b-5). In the Afar, *Lg* is generally efficient except when a path is mostly oceanic (Figs 5b-4, and 6).

Although we occasionally observed clear *Sn* to *Lg* converted phases, for example Mediterranean Sea earthquakes recorded at the HILS station in central Arabia, converted phases were not included in our study. *Lg* blockage was observed through eastern Turkey, the Anatolian Plateau, the southern Black Sea and across the Zagros thrust belts (Fig. 3).

### 3.2 *Sn* observations

Our *Sn* efficiency ray map is shown in Fig. 4. Our *Sn* observations are dense except along the edges and in southeastern Arabia, where

limited stations and ray paths were available. In general, our efficient, inefficient and blocked ray path observations were consistent over the efficiency map. We observed efficient *Sn* propagation in the Mediterranean and the Arabian Platform (Figs 6a-5, 6 and Figs 6b-1, 2, 3 and 6). Efficient *Sn* propagation across the Red Sea was observed at some stations in Saudi Arabia (Figs 5a-1, 2, 3 and 4) as well as *Sn* blockage (Fig. 5a-5 and Figs 5b-1 and 2). Our *Sn* observations in the northern part of the Red Sea (north of 24° latitude) have high-frequency content (Figs 5a-3 and 4). *Sn* was blocked along the Afar Depression, the Dead Sea fault system, and the Anatolian–Iranian Plateau. Also, efficient *Sn* propagation was observed across the Zagros (Figs 6b-3, 4, 5 and 6). We observed inefficient *Sn* propagation for paths crossing southern Yemen (Fig. 5c-2). We have also observed a region of *Sn* attenuation from eastern Iraq to Jordan and northwestern Saudi Arabia (Figs 5c-4 and 6).

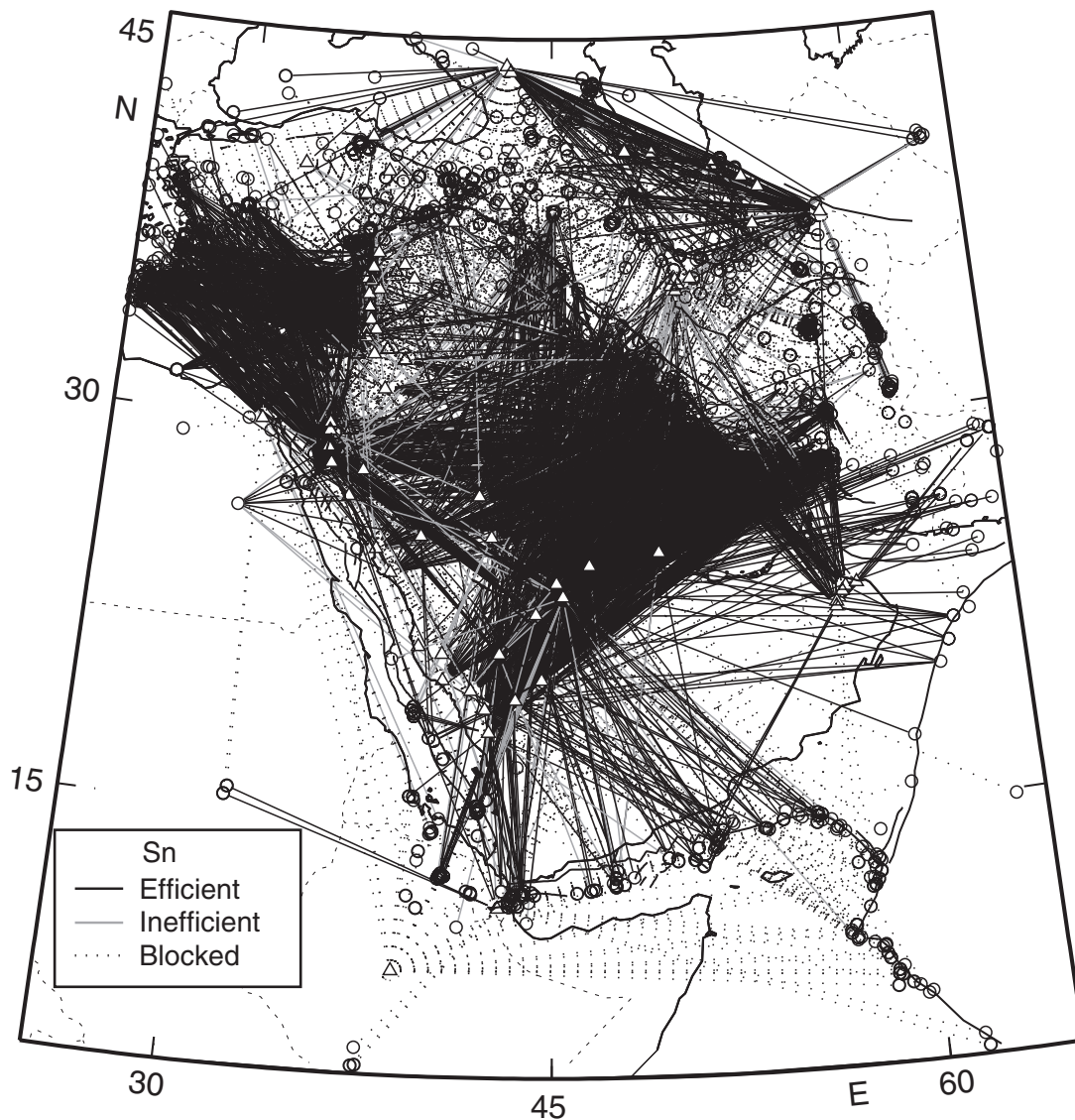


**Figure 4.** Map showing more than 6200  $S_n$  ray path efficiencies. Each ray path corresponds to an earthquake–station pair. The seismograms corresponding to these rays were classified by visible inspection by the authors as efficient, inefficient or blocked. Inefficient and  $S_n$  blockage have been observed along the Dead Sea fault system, the Turkish–Iranian Plateau, Afar and south of the Arabian Plate. Efficient  $S_n$  propagation dominates within most of the Arabian Plate. Efficient as well as blocked and inefficient  $S_n$  ray paths were observed across the Red Sea.

## 4 TOMOGRAPHIC IMAGING OF LG AND SN

### 4.1 $Lg$ tomography

#### 4.1.1 $Lg/Pg$ amplitude ratio tomography method

The  $Lg/Pg$  ratio tomography method used in this study is based on Sandvol *et al.* (2001). This technique is an objective method to map regional phase attenuation. Also, by using the ratio method the values of the ratios are not discrete and therefore contain more information about the details of  $Lg$  attenuation relative to  $Pg$ .

Based on the derivation of Phillips *et al.* (2001) with slight modification, and the convolution model of Cong *et al.* (1996), the amplitude of a given phase as a function of frequency can be expressed by:

$$a_{ijk}(w) = a_{0i}(w)s_{jk}(w)c_{ik}(w)x_{ij}^{(-\beta_k)}(w)\exp(-\alpha_k(w)x_{ij}), \quad (1)$$

where  $i, j$  and  $k$  are the event, station and phase-type indices respectively,  $a_{0i}$  is the total amplitude of the source,  $s_{jk}$  is the response of the station and site,  $c_{ik}$  is the partitioning of the amplitude into a particular phase type,  $x_{ij}$  is the event–station separation,  $\beta_k$  is the spreading coefficient and  $\alpha_k$  is the attenuation factor. The natural log of the amplitude ratios of the two phases  $Lg$  and  $Pg$  (labelled 1 and 2) that follow the same path at a given frequency is:

$$\Delta A_{ij} = \Delta S_j + \Delta C_i - \Delta\beta \log(x_{ij}) - \Delta\alpha x_{ij}, \quad (2)$$

where

$$\Delta A_{ij} = \log(a_{i1}/a_{i2}),$$

$$\Delta S_j = \log(s_{j1}/s_{j2}),$$

$$\Delta C_i = \log(C_{i1}/C_{i2}),$$

$$\Delta\beta = (\beta_1 - \beta_2),$$

$$\Delta\alpha = (\alpha_1 - \alpha_2)$$

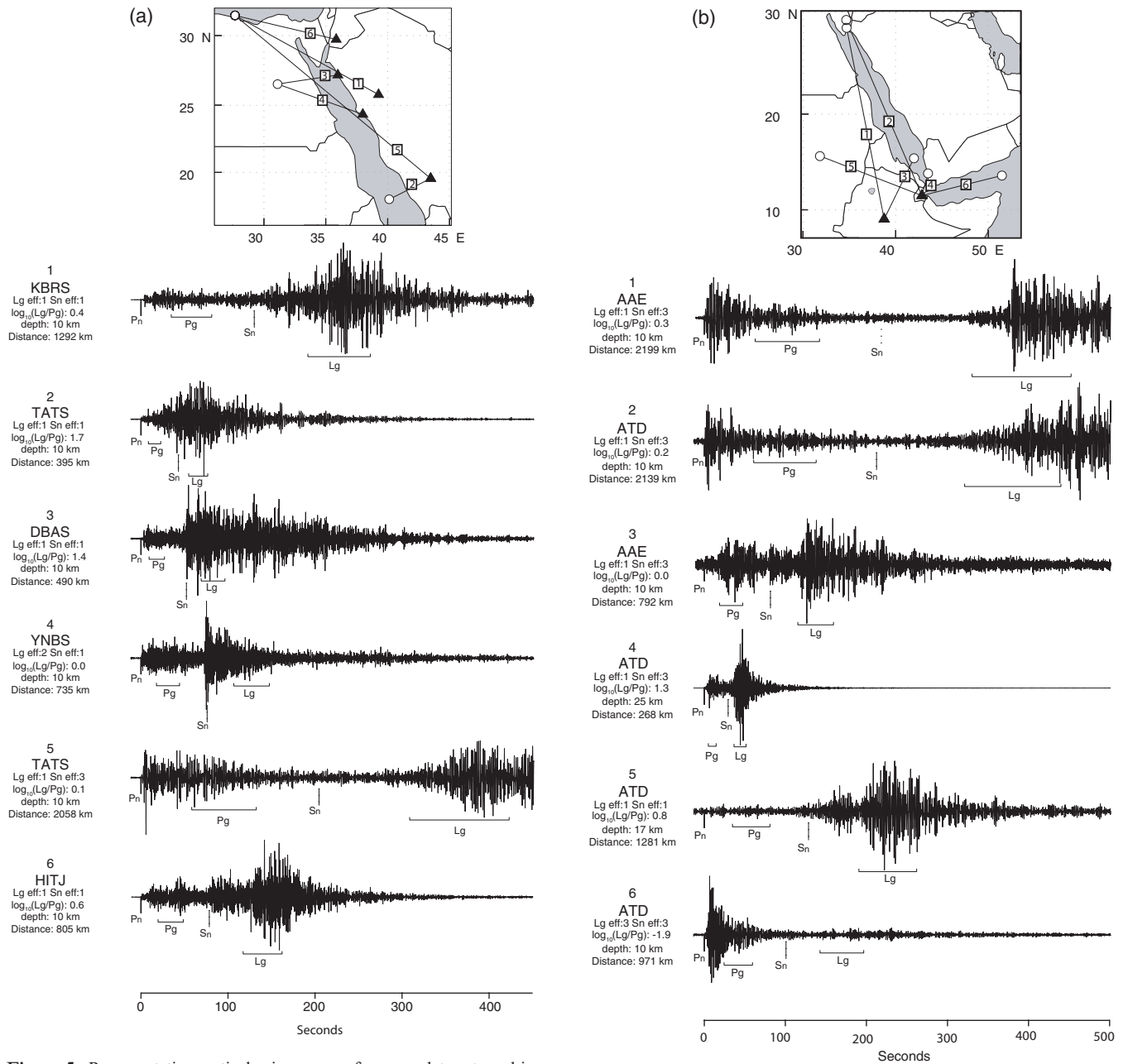


**Figure 5.** Representative vertical seismograms from our data set used in this study and classified efficiencies. Earthquakes are marked by circles and stations by triangles. All waveforms were band passed from 0.5 to 5.0 Hz. Waveforms are numbered and labelled by station name, observed Lg and Sn efficiencies,  $\log_{10}$  of (Lg amplitude/Pg amplitude), depth and the distance from the station. The selected Pn is shown by a solid line. The predicted Sn arrival time relative to the first arrival assuming a crustal thickness of 35 km and a crustal S velocity of 3.6 km s<sup>-1</sup> and a mantle S velocity of 4.5 km s<sup>-1</sup> is marked by the dotted line. Velocity windows of 5.2–6.2 km s<sup>-1</sup> for Pg and 3.1–3.6 km s<sup>-1</sup> for Lg are shown. (a) Rays crossing the Red Sea showing the diverse pattern in Sn and Lg efficiencies. (b) Rays along the Red Sea and across East Africa showing Sn blockage along the Red Sea and Gulf of Aden. Lg rays were efficient along the Red Sea. The traveltimes for these Lg phases corresponds to direct ray path propagation. Lg blockage was observed along the Gulf of Aden. (c) Ray paths for an event in northern Iraq and in the Gulf of Aden at different stations within the Arabian Plate. Inefficient propagation and Sn blockage was observed in a region southeast of Syria and northwest of Jordan, and west of Yemen. Inefficient Lg was observed along the Mesopotamian Foredeep.

**Figure 5.** (Continued.)

Assuming the event–station separation  $x_{ij}$  to consist of a number of line segments  $x_{ijm}$  with a differential attenuation constants  $\Delta\alpha_m$  eq. (2) can be rewritten as:

$$\Delta A_{ij} = \Delta S_j + \Delta C_i - \Delta\beta \log(x_{ij}) - \sum_m \Delta\alpha_m x_{ijm}, \quad (3)$$

To invert for the variables in eq. (3) two assumptions were made. First, the site and seismometer response to the two phases is absorbed in the  $\Delta C$  term. Second, the relative ratio of the two phases is independent of the source size, depth and location and thus  $\Delta C$  is constant. For this study a 35 km cut-off in depth for the Lg/Pg ratio tomography was applied to reduce the effect of the second assumption. Substituting

$$\Delta\alpha_m = \Delta\alpha + \Delta\alpha'_m \Delta\alpha,$$

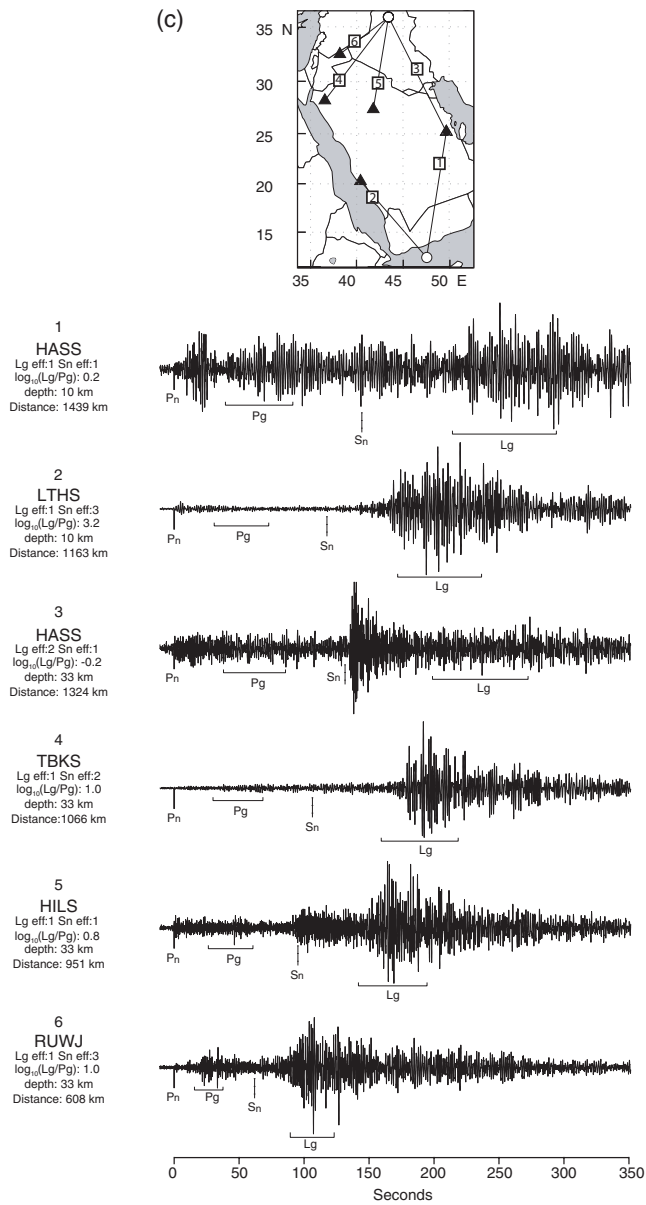


Figure 5. (Continued.)

in eq. (3) where  $\Delta\alpha$  is the mean differential attenuation and  $\Delta\alpha'_m$  is the perturbation in differential attenuation along ray segment  $m$ , eq. (3) can be rewritten as:

$$\Delta A_{ij} = \Delta C - \Delta\beta \log(x_{ij}) - \Delta\alpha - x_{ij} - \sum_m \Delta\alpha'_m x_{ijm}. \quad (4)$$

The distance dependence of  $Lg/Pg$  amplitude ratios has been accounted for in our study by the variable  $\Delta\beta$ . Fig. 7 shows all the  $Lg/Pg$  amplitude ratios versus distance for all the data used in this study. Only weak distance dependence was found in our data set, primarily because of substantial blockage attenuation that both  $Lg$  and  $Pg$  undergo over the study area. By solving for  $\Delta C$ ,  $\Delta\beta$  and  $\Delta\alpha$  using non-linear curve fitting and applying these corrections, eq. (4) can be rewritten as:

$$\begin{aligned} \Delta A'_{ij} &= \Delta A_{ij} - \Delta C - \Delta\beta \log(x_{ij}) + \Delta\alpha x_{ij} \\ &= \sum_m \Delta\alpha'_m x_{ijm}, \end{aligned} \quad (5)$$

where  $\Delta A'_{ij}$  is the corrected log amplitude ratio. Based on eq. (5) we applied a linear tomographic inversion for the corrected amplitude

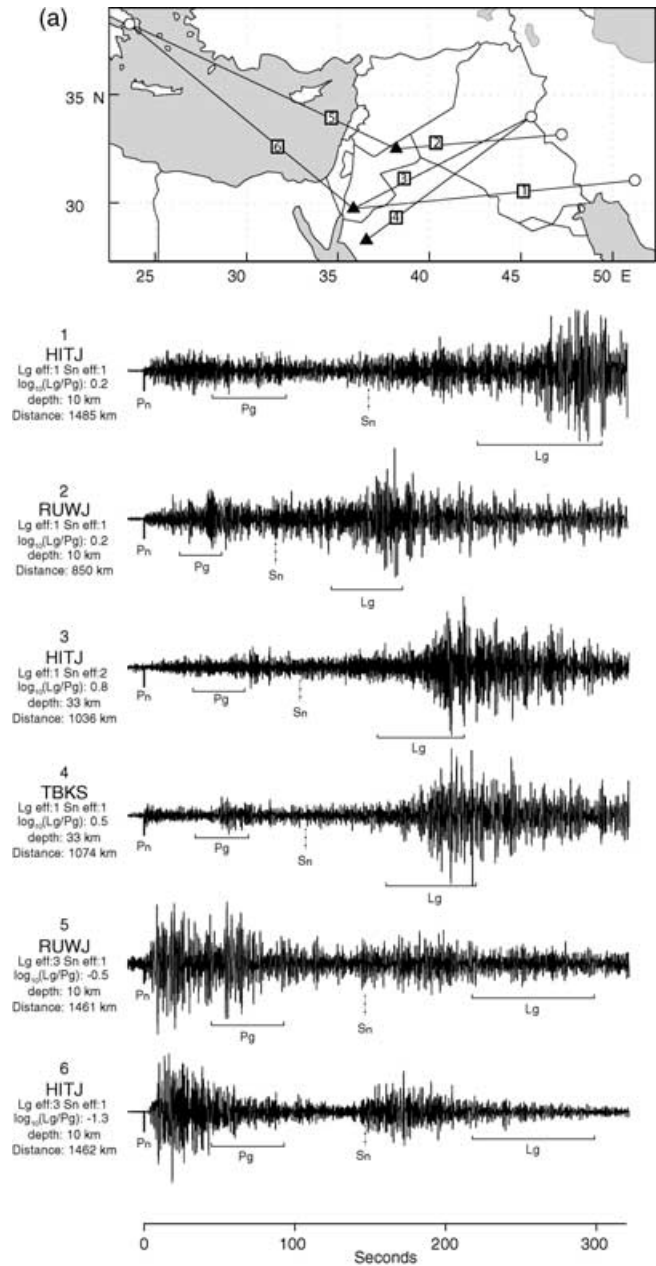


Figure 6. Representative vertical seismograms from our data set used in this study and classified efficiencies. Earthquakes are marked by circles and stations by triangles. All waveforms were band passed from 0.5 to 5.0 Hz. Waveforms are numbered and labelled by station name, observed  $Lg$  and  $Sn$  efficiencies,  $\log_{10}$  of ( $Lg$  amplitude/ $Pg$  amplitude), depth and the distance from the station. The selected  $P_n$  are shown by a solid line. The predicted  $Sn$  arrival time relative to the first arrival assuming a crustal thickness of 35 km and a crustal  $S$  velocity of  $3.6 \text{ km s}^{-1}$  and a mantle  $S$  velocity of  $4.5 \text{ km s}^{-1}$  is marked by the dotted line. Velocity windows of  $5.2\text{--}6.2 \text{ km s}^{-1}$  for  $Pg$  and  $3.1\text{--}3.6 \text{ km s}^{-1}$  for  $Lg$  are shown. (a) Inefficient  $Lg$  propagation was observed in the Mediterranean Sea. Efficient  $Lg$  propagation was observed for ray paths from Zagros crossing Iraq. Low-frequency efficient  $Sn$  propagation was observed in eastern Jordan. (b) Efficient  $Sn$  and  $Lg$  paths from Zagros to Jordanian and Saudi stations.  $Lg$  blockage was observed for paths crossing Zagros. (c)  $Lg$  was mostly blocked or attenuated at Oman stations; however, efficient  $Sn$  was observed at the same stations.

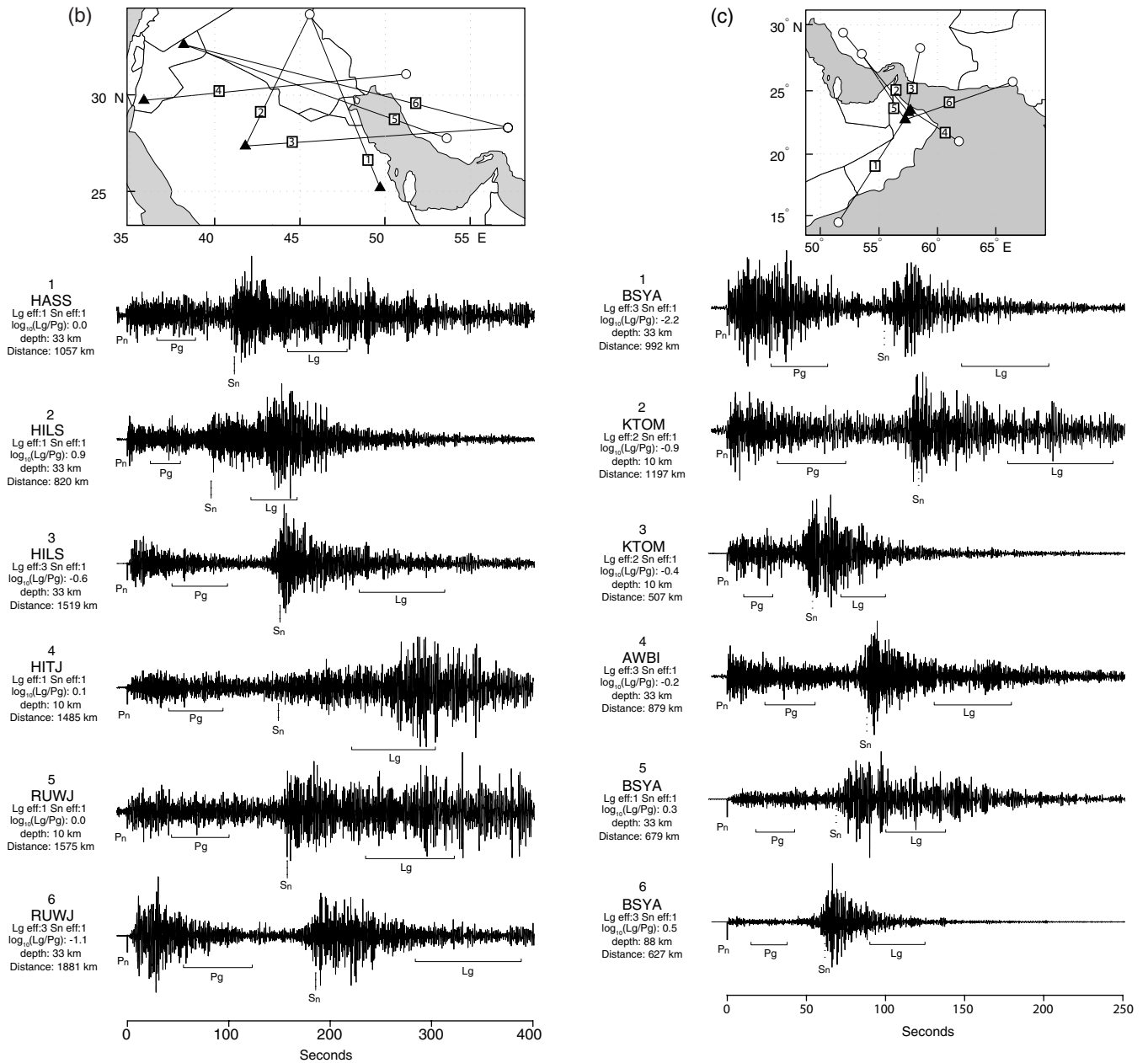


Figure 6. (Continued.)

ratios to determine the lateral variation in  $\Delta\alpha'_m$ . The programs for solving the inversion were originally written for *Pn* velocity tomography by Hearn & Ni (1994) and modified by Sandvol *et al.* (2001) to solve for *Lg/Pg* ratio tomography. The equations were solved using the LSQR algorithm (Paige & Saunders 1982). The inversion steps are detailed in Calvert *et al.* (2000).

4.1.2 Results

Our *Lg* propagation relative to *Pg* for a cell size of  $0.5^\circ$  depicted in Fig. 8(a) outlines areas where *Lg* is efficient, inefficient or blocked. The model is dominated by regions of efficient and blocked *Lg*, buffered by regions of inefficient *Lg*. The main tectonic area where efficient *Lg* propagation is clearly observed is along the Arabian Shield, consistent with other studies (e.g. Sandvol *et al.* 2001;

Figure 6. (Continued.)

Mellors *et al.* 1999; Cong & Mitchell 1998). In general, *Lg* is less efficient in the platform than in the shield. In our *Lg/Pg* model, *Lg* is efficient along the DSFS and in Jordan, Syria and Iraq. An inefficient *Lg* region was observed in Oman. West of the Arabian Shield and across the Red Sea we observed another *Lg*-efficient zone spreading from southern Egypt to northern Ethiopia and connected to the Arabian Shield across the Red Sea. Two main regions of inefficient *Lg* propagation can be identified in the Red Sea. The first one is along the northwestern shoreline of the Red Sea and the second one is in the southwestern part of the Red Sea along the Danakil Depression. This anomaly is connected to the Afar Depression and the Gulf of Aden. Southwest of Afar efficient *Lg* propagation was observed. In general, we observed *Lg/Pg* blockage across the Mediterranean, the Turkish and Iranian plateaus, the Zagros thrust belt, south of the Caspian Sea, Makran and in the Gulf of Oman. These constitute a continuous region of *Lg* attenuation. *Lg* was efficient in the northern part of the Caspian Sea.

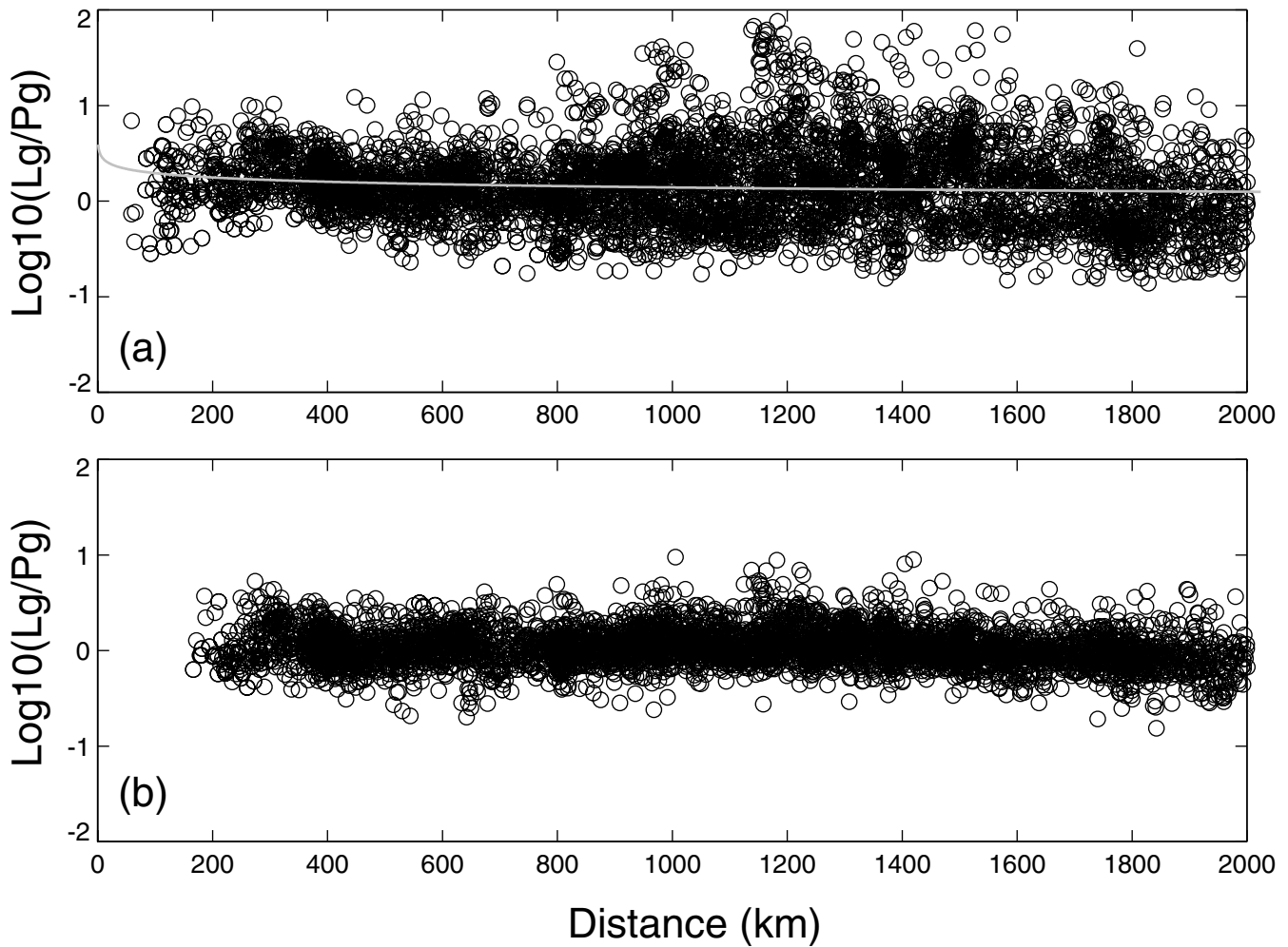


**Figure 7.** (a)  $\text{Log}_{10}$  of the  $L_g$  amplitude/ $P_g$  amplitude versus distance for each path in Fig. 3. The line in panel (a) is the best fit for the logarithm of the distance. (b) Shows the residual after 12 iteration using a Laplacian damped LSQR algorithm. There is a reduction in the variance of  $L_g/P_g$  ratio using our tomographic model.

## 4.2 $S_n$ propagation efficiency tomography

### 4.2.1 Method

In mapping the  $S_n$  propagation, we were required to use a modified version of amplitude ratio tomography due to the fundamental difference in  $S_n$  propagation in continental and oceanic lithosphere. Amplitude ratios of the  $S_n$  phase to  $P_n$ ,  $P_g$  or the whole  $P$  window were less successful in mapping variation in lithospheric attenuation structure than  $S_n$  efficiency tomography (Rodgers *et al.* 1997; Calvert *et al.* 2000). Our  $S_n$  efficiency tomography is based on our qualitative observations mentioned in Section 3.2. The tomographic method uses a modified version of eq. (4) above with the main assumption that phase 1 is the observed  $S_n$  amplitude and phase 2 is the  $S_n$  amplitude that would be observed if there was a constant attenuation factor of  $\alpha_2$  along the path. In essence, by categorizing the phases into qualitative bins, we are essentially attempting to correct for  $\Delta S_j$ ,  $\Delta C_i$  and  $\Delta\beta$  terms, which lead to the following equation:

$$\begin{aligned} \Delta A_{ij} &= \log(a_{ij1}/a_{ij2}) \\ &= \sum_m (\alpha_2 - \alpha_{1m}) x_{ijm} = \sum_m \alpha_m x_{ijm} \end{aligned} \quad (6)$$

If we assume  $\alpha_2$  to correspond to the attenuation for an efficient path,  $\Delta A$  would be zero since  $\log(1) = 0$ . For a blocked path of

$\Delta A_{ij\text{block}}^{\text{obs}}$ , an arbitrary log amplitude ratio was assumed, as well as a variable value  $k \Delta A_{ij\text{block}}^{\text{obs}}$  [ $0 < k < 1$ ] for the inefficient paths. If we normalize the model parameters by dividing by  $\Delta A_{ij\text{block}}^{\text{obs}}$  (eq. 7) the model parameter  $\alpha_m$  would be independent of the choice of  $A_{ij\text{block}}^{\text{obs}}$ :

$$\alpha_m^{\text{norm}} = (\alpha_m) / (\Delta A_{ij\text{block}}^{\text{obs}}). \quad (7)$$

In general,  $k$  is a parameter by which the inefficient observation can be weighted more closely to efficient or blocked to get the best possible representation of the data. Since the inefficient paths are small in number compared with the efficient and blocked paths, the  $k$  parameter has a small and limited impact on the resulting model. We have rigorously tested the effect of  $k$  on our model; the effect is largest in regions with poor ray coverage. In Fig. 8(b) we have chosen a cell size of  $0.5^\circ$ ,  $k = 0.6$  and a damping of 0.6 after several trials that for the sake of brevity have not been included.

### 4.2.2 Results

$S_n$  propagation or blockage reflects the rheology of the mantle lid. At very short distances, however, the crustal legs of  $S_n$  may also affect  $S_n$  phase amplitude. The  $S_n$  tomography model presented in Fig. 8(b) clearly corresponds to the major tectonic boundaries in

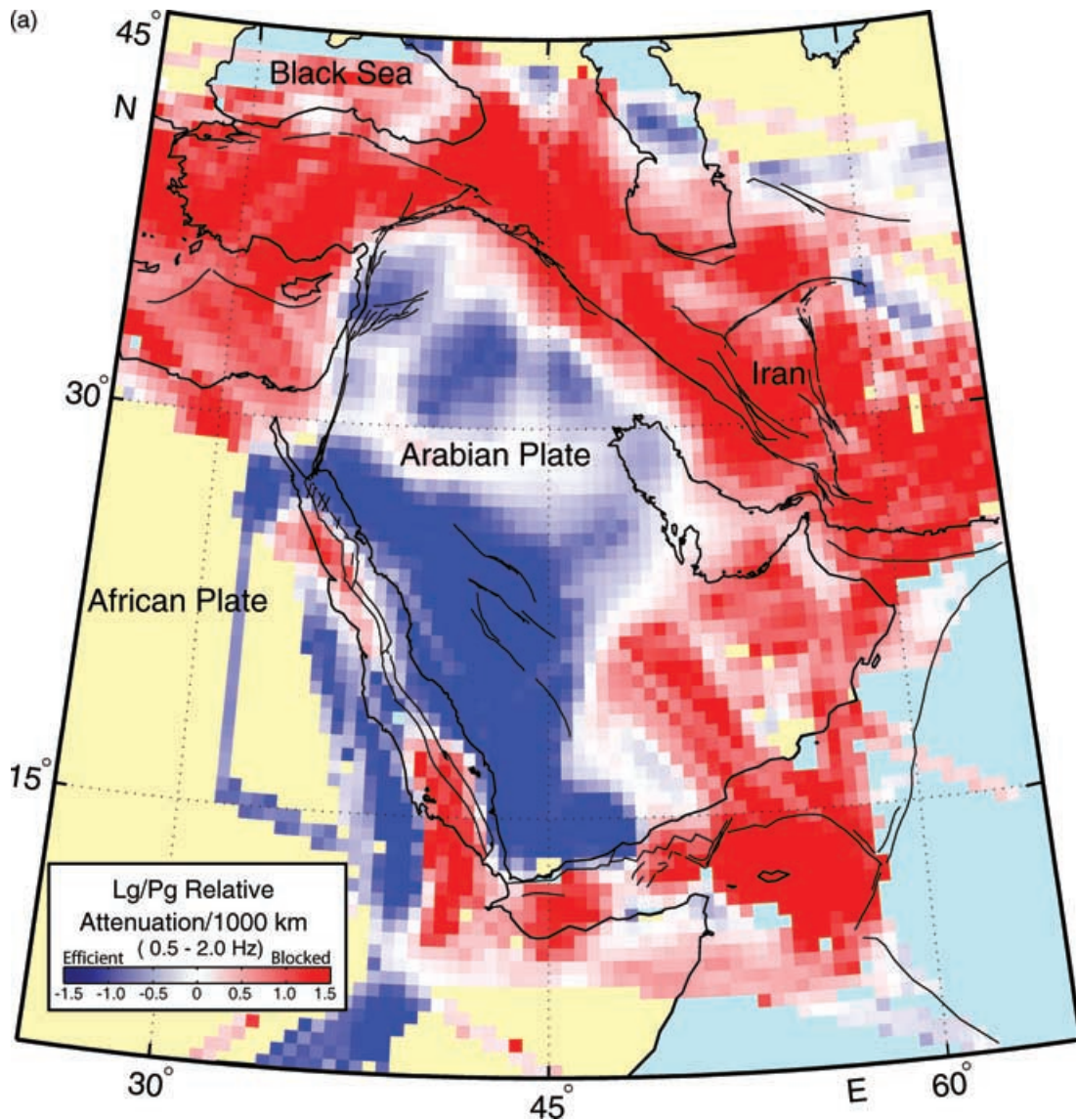


**Figure 8.** Two maps showing our  $Lg/Pg$  ratio tomography and  $S_n$  tomography overlaid by the main faults and tectonic boundaries in the region. (a) Map showing the  $Lg/Pg$  ratio tomography for the Arabian Plate and surrounding regions.  $Lg$  is efficient in the Arabian Plate and some parts of the Red Sea.  $Lg$  blocked across the Zagros, Turkish and Iranian plateaus, the Mediterranean Sea, the Gulf of Aden and the Afar region. The southeastern part of the Arabian Platform is dominated by a leakage in tomography due to blockage in the Arabian Sea (see Fig. 3). (b) Map showing the  $S_n$  tomography for the same region. Inefficient  $S_n$  propagation and blockage are mostly along the Dead Sea fault system and nearby regions, the Turkish and Iranian plateaus, part of the Red Sea, eastern Yemen, the Gulf of Aden and the Afar region. The tomography also shows smaller regions of inefficient  $S_n$  in the margins of the Arabian Shield.  $S_n$  is efficient in the Mediterranean Sea, Black Sea and Caspian Sea.

the study region.  $S_n$  is inefficient or blocked along the Dead Sea fault system, Turkey, the Iranian Plateau, the Arabian Sea, the Gulf of Aden and the Afar Depression.  $S_n$  is efficient, however, in the Mediterranean Sea, the southern part of the Caspian Sea, most of the Arabian Platform and most of the Arabian Shield. Inefficient  $S_n$  propagation was observed in the northwestern part of the Arabian Platform, for example in Syria, Jordan and northwestern Iraq. Also, inefficient  $S_n$  propagation was observed in areas correlating well with Neogene/Quaternary volcanic activity in the Arabian Shield. Along the Red Sea we observed a variable pattern of  $S_n$  efficiency. Regions of blocked or inefficient  $S_n$  were observed in the northern part, along the eastern coastlines and between the Danakil Depression and western coastlines of the Red Sea. Efficient  $S_n$  was observed across the central Red Sea.

Two continuous regions of high  $S_n$  attenuation were observed. The first region extends along the Afar Depression and the Gulf of Aden leading to the Owen fracture zone. The second region is along the Dead Sea fault system, Turkey and the Iranian Plateau. In comparison with  $Lg$  propagation,  $S_n$  is efficient along the northern Zagros thrust belt down to the western part of Makran and the Gulf of Oman. The eastern edge of the  $S_n$ -efficient zone correlates well with the mapped Zagros suture zone. North of the Iranian Plateau efficient  $S_n$  propagation was observed in Kopet Dagh, the Caspian Sea and the northeastern part of the Caucasus mountains.

#### 4.3 Resolution and uncertainties

The distribution of stations and sources plays an important role in resolving the seismic characteristics of the ray paths in between.

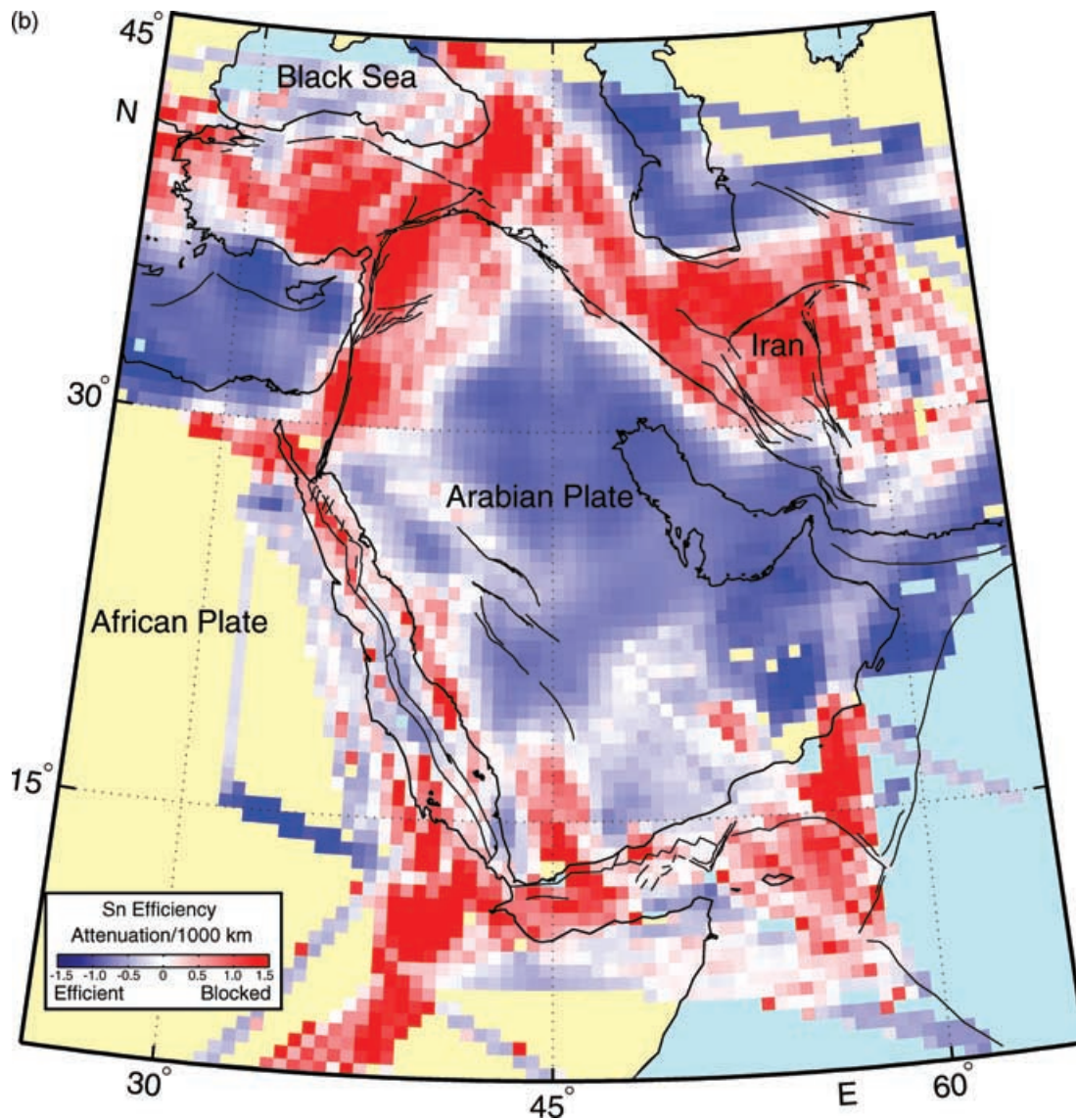


Figure 8. (Continued.)

A good ray path distribution is needed to accurately map propagation in a region. Unfortunately, control over the source and station distribution is fairly limited when passive seismic sources are used, resulting in variation of imaging quality over the imaged area. Two resolution tests have been applied to our tomographic models, the synthetic checkerboard and spike tests. For the  $Lg/Pg$  ratio study we added Gaussian noise of  $\pm 15$  per cent of the maximum synthetic  $Lg/Pg$  ratio. We used the bootstrap resampling technique to further test the stability of our model. In this statistical analysis technique we simply resample our data until we reach the same number of observations as in our original inversion and then we invert the resampled data for a model. We repeat this process 100 times to draw a variance to detect any regions of the model that are dependent on only a few inconsistent observations (Hearn & Ni 1994).

Our  $Lg$  hit map, which shows the number of rays passing through each cell of our tomography, is shown as an electronic supplement to this paper. The map shows cells of dense ray coverage and cells having limited or no ray coverage. In general, most regions covered by our  $Lg$  model are well covered except in the southeastern

part of the Arabian Platform and the Red Sea. We also performed the bootstrap test on our  $Lg/Pg$  data set following a method similar to that used by Sandvol *et al.* (2001) and Calvert *et al.* (2000). Our  $2\sigma$  bootstrap (see the electronic supplement) shows high uncertainty along the model edges, such as the Red Sea, the Gulf of Aden, Egypt and eastern Iran. We also observed high uncertainty in Afar and in the southeastern part of the Arabian Platform. Regions with high uncertainty mostly coincide with regions of limited ray coverage. The main goal of the checkerboard test is to point to weaknesses in the model by generating synthetic efficiency data. In this procedure we divide the study area into squares of blockage and efficient areas in a pattern similar to a checkerboard (Fig. 9). The initial checkerboard model for the  $Lg/Pg$  ratio study is shown in Fig. 9 and our test model is shown in Fig. 10. We used  $5^\circ \times 5^\circ$  checkerboard cells covering all the regions where ray paths were available. Our  $Lg/Pg$  checkerboard test results in Fig. 10 show areas where ray paths were limited in number, for example where ray coverage density is low, or confined to one direction. These two conditions resulted in smearing or a poor recovery of the original model. We observed leakage in areas lacking dense coverage (see Fig. 9) such as the southeastern

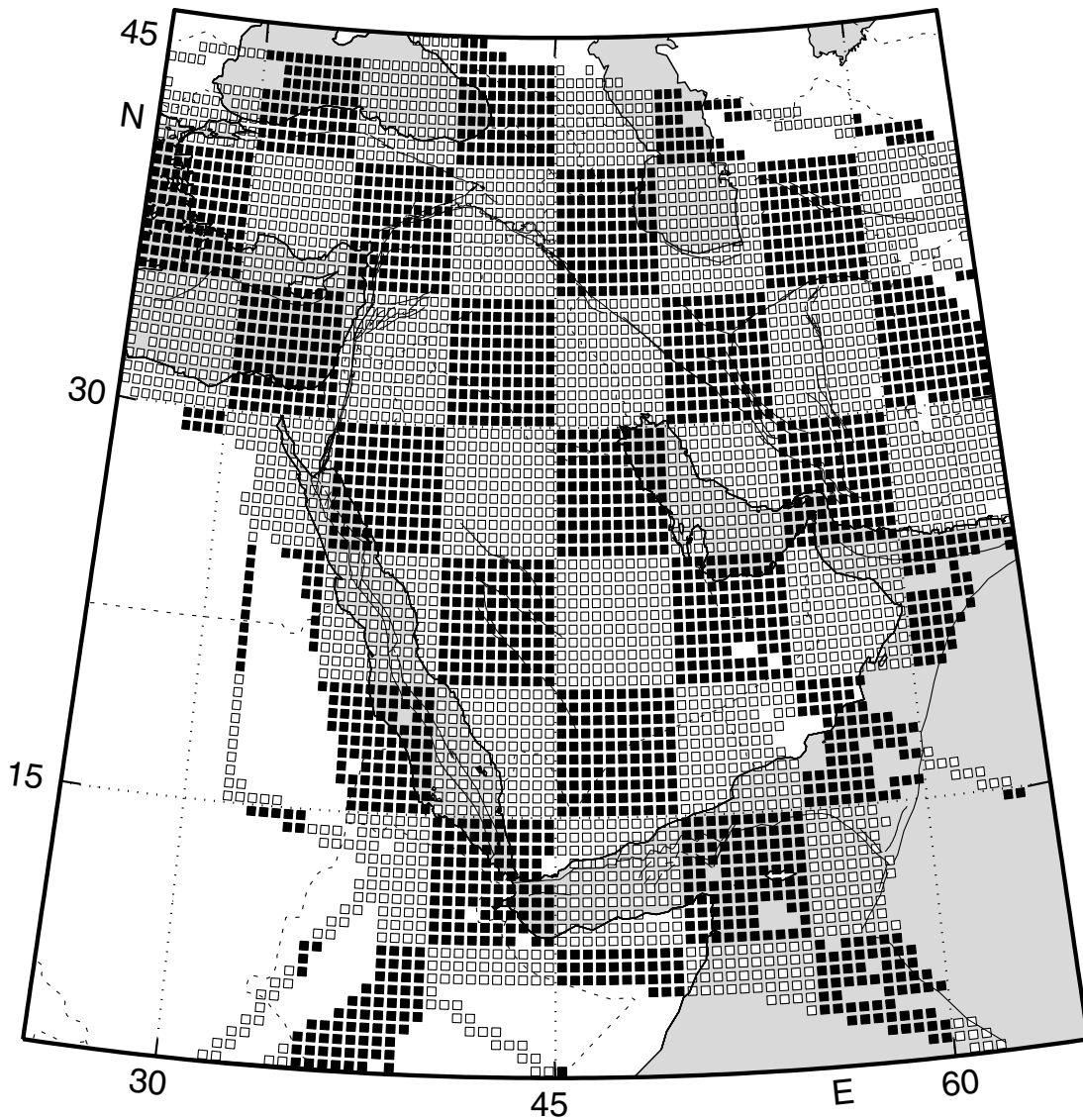


Figure 9. Map showing the original checkerboard input used to generate the  $Lg/Pg$  synthetic ratios.

part of the Arabian Platform, Afar and along the Red Sea. We also observed smearing in regions where most ray paths were confined to one direction, such as the Arabian Platform, Yemen, eastern Iran, Afar and in the Mediterranean Sea. We observed good recovery in the Arabian Shield, the Iranian Plateau, Anatolia, the southern Caspian Sea and in Syria.

We performed similar tests on our  $S_n$  data set. Our  $S_n$  hit map (see the electronic supplement) shows limited ray coverage in the southeastern part of the Arabian Platform and along the Red Sea. In our  $2\sigma$   $S_n$  bootstrap results (see the electronic supplement) we observed regions with high uncertainty along the model edges, such as the Red Sea, the Gulf of Aden, Egypt and eastern Iran. We also observed high uncertainty in Afar and in the southeastern part of the Arabian Platform. We performed the spike test on our  $S_n$  data set. Our initial spike test model is shown in Fig. 11 and the test result is shown in Fig. 12. We used  $4^\circ \times 4^\circ$  cells covering all the regions where ray paths were available. A 300 km blockage path length was assigned to our  $S_n$  test attenuation zones. We used the same ray paths as in our tomographic model to generate synthetic data. If a ray spent more than the blockage extension path length in a

blockage area it was marked as blocked. Only efficient and blocked synthetics were generated. By switching 10 per cent of the blocked to efficient, and vice versa, we added noise to our synthetic test. Our  $S_n$  spike test results in Fig. 12 shows regions of good recovery and poor recovery in our  $S_n$  model. We observed leakage in areas lacking dense coverage (see Fig. 4) such as the southeastern part of the platform. We also observed smearing in regions where most ray paths were confined to one direction, such as Afar, the Gulf of Aden, the northern part of the Arabian Shield, Yemen, eastern Iran and the Mediterranean Sea. We observed good recovery in the Arabian Platform, the Iranian Plateau, Anatolia, the southern Caspian Sea and in Syria.

## 5 PN ATTENUATION

The  $P_n$  phase is a mantle lid guided wave and it is the first phase to arrive when the distance between a station and an earthquake exceeds about 150 km in continental regions with a Moho depth of about 35 km. The velocity, amplitude and frequency of the  $P_n$  phase depend on the rheology of the sampled path. The reverse

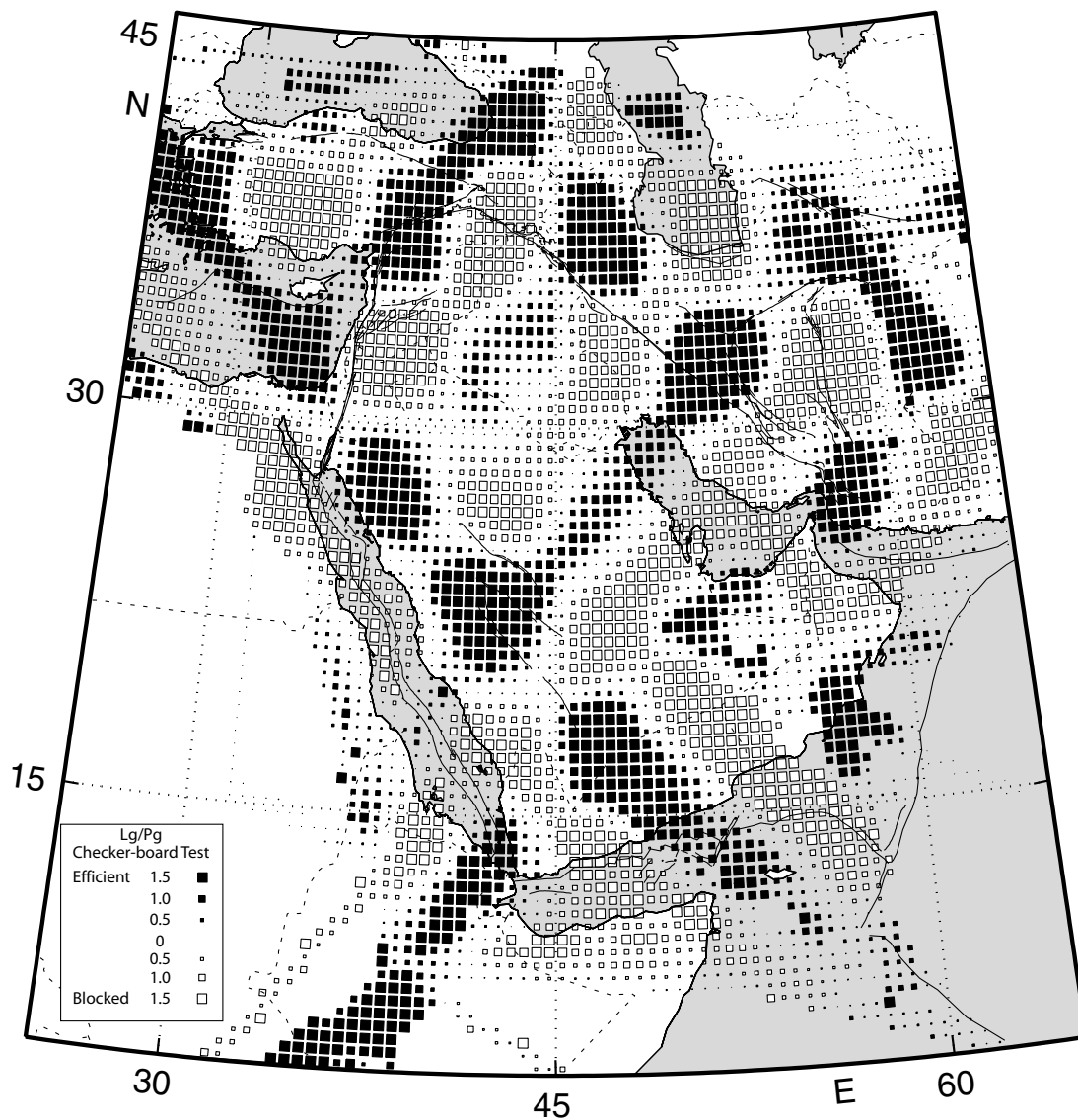


**Figure 10.** The recovered checkerboard showing well-recovered regions and regions vulnerable to leakage or smearing in our  $Lg/Pg$  model. Smearing or leakage occurs due to limitations in the distribution of earthquakes and stations. Regions vulnerable to smearing are Zagros, the Arabian Platform, eastern Turkey and the Mediterranean Sea. Regions vulnerable to leakage are Afar and the southeastern Arabian Platform. Well recovered regions are the Arabian Shield, the Turkish–Iranian Plateau and the northern Arabian Platform.

two-station method (RTSM) (see inset in Fig. 13) isolates the effect of the upper mantle leg from the effect of the crustal leg and the station response. In this study the attenuation factor  $Q_{Pn}$  has been determined in four regions (see Fig. 13). The RTSM has been used to estimate  $Q_{Pn}$  in three different regions, namely Syria, the eastern part of the Arabian Shield and the western part of the Arabian Shield. In the Arabian Platform, where stations and azimuthal data coverage are limited, we used the simple two-station method (TSM) (see inset in Fig. 13).

### 5.1 The reverse two-station method

The RTSM was first introduced by Chun (1986) and Chun *et al.* (1987) to estimate  $Q_{Lg}$  for eastern Canada. The method was based on a pre-assumed value for the geometrical spreading rate coefficient. This assumption would jeopardize the accuracy of the results if

the method were used to estimate  $Q_{Pn}$  (Hill 1973; Sereno 1989). By developing a method to solve for the spreading rate coefficient and  $Q_{Pn}$  simultaneously, Zhu *et al.* (1991) used the RTSM method to determine  $Q_{Pn}$ . The method is based on the availability of four recordings of two earthquakes lining up with two stations, where the stations fall between the earthquakes (Zhu *et al.* 1991). To solve for  $Q_{Pn}$  we used the following equation of Zhu *et al.* (1991):

$$\gamma(f) = \pi f / V_p Q_{Pn}(f),$$

where  $\gamma$  is the attenuation coefficient,  $f$  is frequency and  $V_p$  is the assumed velocity for  $Pn$ . We assumed a  $Pn$  velocity of  $7.9 \text{ km s}^{-1}$ .

### 5.2 Data

The waveform data used to estimate  $Q_{Pn}$  were selected from the database for  $Lg$  and  $Sn$  attenuation. The data were selected according to signal-to-noise ratio, alignment with two recording stations

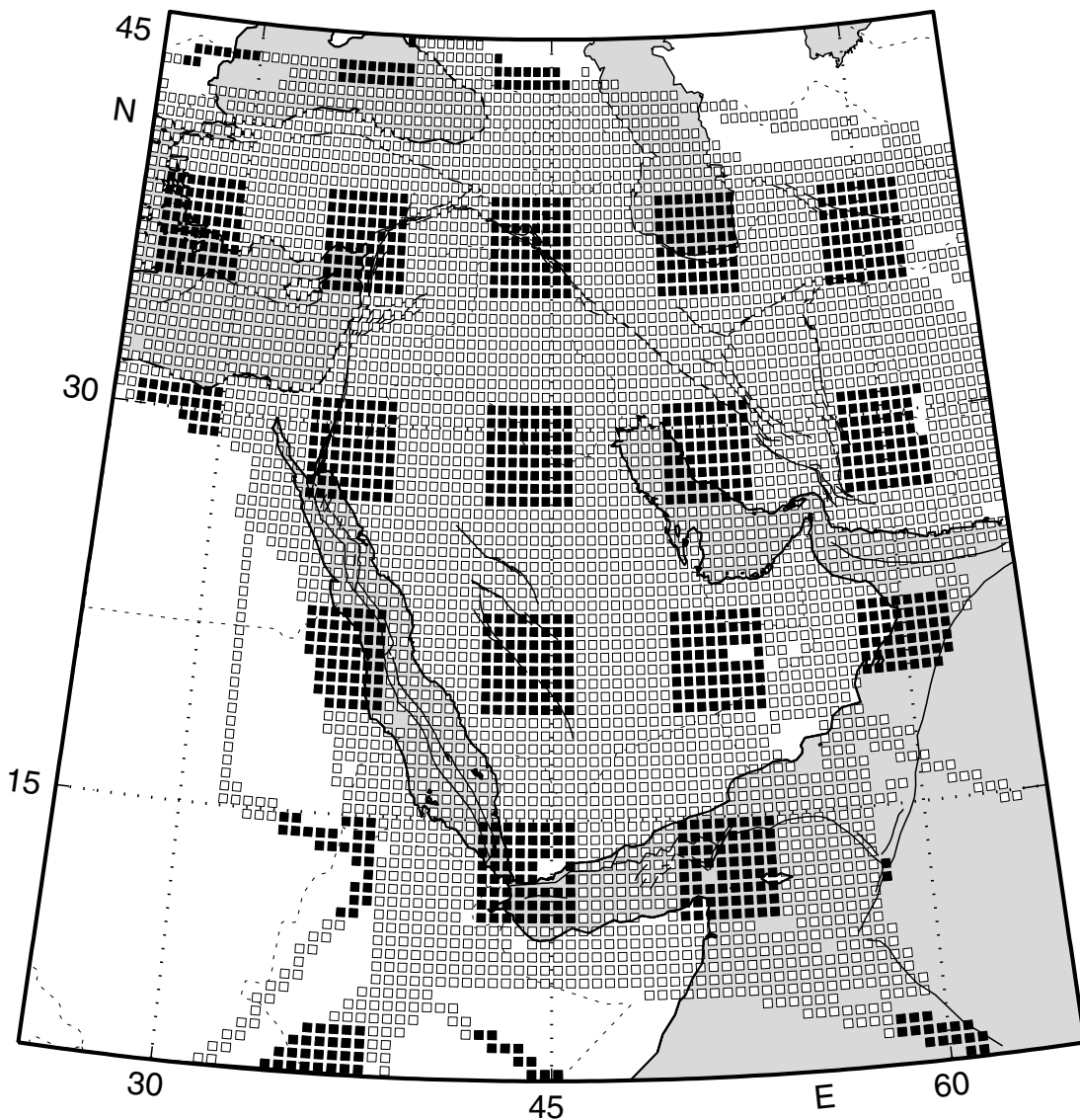


Figure 11. Map showing the original checkerboard input used to generate  $S_n$  synthetic efficiencies.

separated by a distance of more than 100 km and the availability of another event corresponding to a reversed path. Also, we allowed an azimuthal variance of  $6^\circ$  or less. The signal, which consists of 10 s of  $P_n$  window starting from the first arrival, and the noise, which consists of a 10 s window before the onset of the  $P_n$ , was cut after filtering and the ratio of the root mean square (RMS) of the amplitudes was taken. The combination was used only when the RMS ratio of the signal-to-noise exceeded 2. We used a multitapering technique to estimate the power spectral density of the time series and in determining the  $Q_{P_n}$  (Park 1987). To apply the RTSM, an earthquake in the opposite direction from the stations and satisfying the same above criteria is required. Fig. 13 shows all the earthquake combinations used to estimate  $Q_{P_n}$  values for this study. Fig. 14 shows examples of  $P_n$  waveforms using the RTSM approach.

### 5.3 Results for $Q_{P_n}$

The  $Q_{P_n}$  values estimated using RTSM and TSM (Fig. 15) were in good agreement with our  $S_n$  attenuation results. In the Arabian

Shield, the  $Q_{P_n}$  values in the western part were lower than the  $Q_{P_n}$  values in the eastern part, reflecting higher attenuation in the western part as was shown by the  $S_n$  tomographic model. For example, for a frequency of 1.5 Hz, we observed  $Q_{P_n}$  values of 22 and 465 for the western Arabian Shield and the eastern Arabian Shield respectively. The  $Q_{P_n}$  values of the Arabian Platform were slightly lower than the  $Q_{P_n}$  values of the eastern part of the shield. The lowest observed  $Q_{P_n}$  values were in Syria, where  $Q_{P_n}$  was 15 for a frequency of 1.5 Hz. This is also consistent with the low  $P_n$  velocity values reported by Al-Lazki *et al.* (2003) and our  $S_n$  attenuation model.

For the Arabian Shield, our estimated  $Q_{P_n}$  values are comparable with the  $Q_{P_n}$  results for eastern Canada estimated by Zhu *et al.* (1991) using RTSM. For a frequency of 1.5 Hz the  $Q_{P_n}$  value for eastern Canada was 269. Averaging our  $Q_{P_n}$  values for the shield for the same frequency, we would obtain a  $Q_{P_n}$  value of 244, which is comparably close to the  $Q_{P_n}$  value in eastern Canada. Using the spectral amplitude ratio and pulse broadening techniques the  $Q_{P_n}$  values determined by Badri & Sinno (1991) in the eastern Arabian Shield range from 475 to nearly 1560 for the frequency range between 2 and 12 Hz. Considering our frequency window (1–2 Hz)

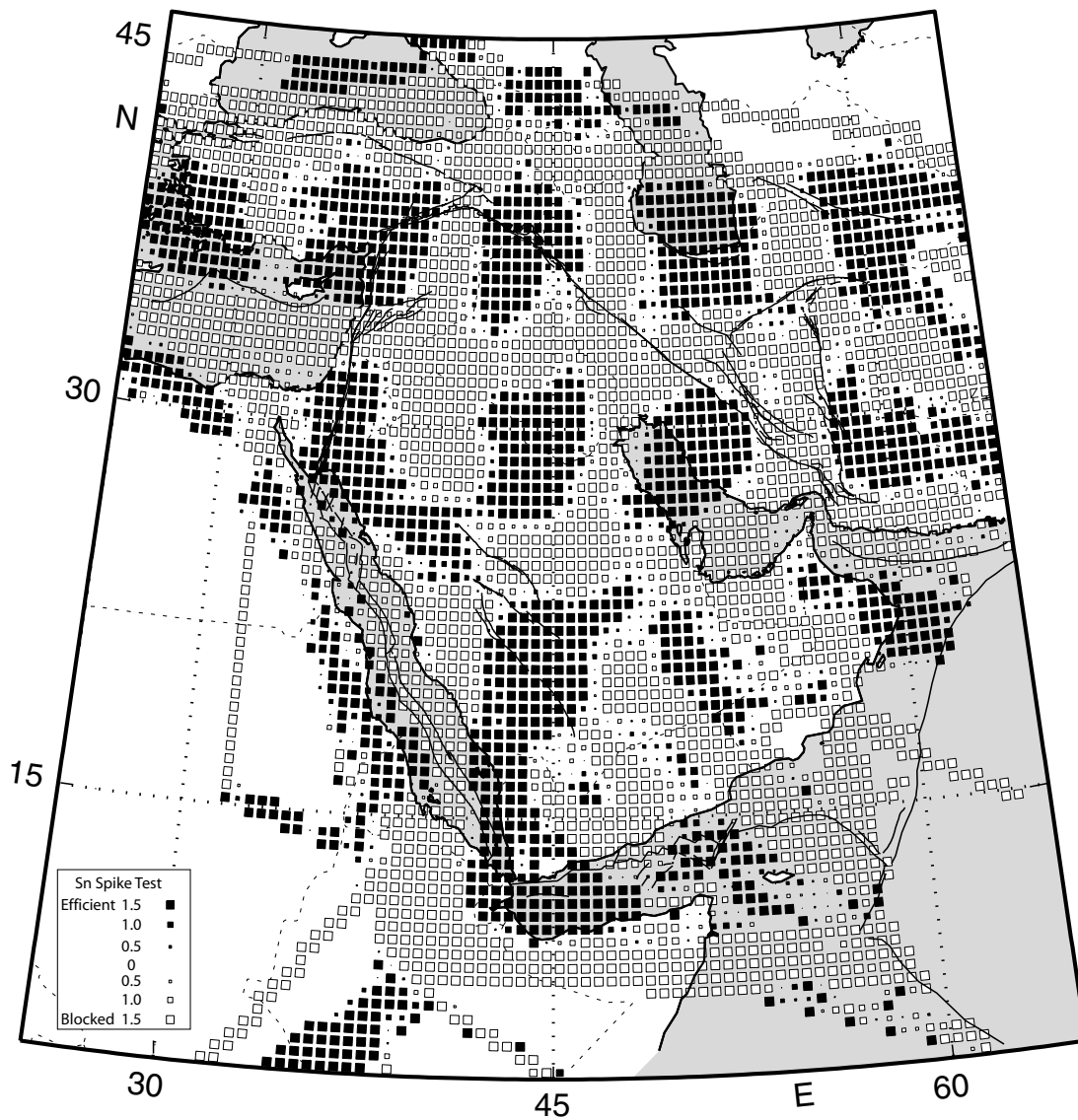


**Figure 12.** The recovered checkerboard showing well-recovered regions and regions vulnerable to leakage or smearing in our  $S_n$  model. Regions vulnerable to smearing are south of the Arabian Shield and the Mediterranean Sea. Regions vulnerable to leakage are Afar and the southeastern Arabian Platform. Well-recovered regions are Zagros, the Arabian Platform and the Turkish–Iranian Plateau.

our  $Q_{Pn}$  results for the eastern part of the shield are comparable with their  $Q_{Pn}$  values.

## 6 DISCUSSION AND CONCLUSIONS

Using a large number of regional seismograms we have been able to map regional seismic wave ( $Lg$  and  $S_n$ ) attenuation in the Arabian Plate and the surrounding regions (Figs 8a and b). The results shown in Figs 8(a) and (b) represent the most comprehensive and complete mapping of  $Lg$  and  $S_n$ . The  $Lg$  seismic phase is a crustal guided wave sensitive to crustal thickness variations and/or intrinsic attenuation. In our  $Lg$  tomographic model (Fig. 8a), a distinctive  $Lg$  blockage zone extends from Makran, southeast of the Arabian Plate, along the Zagros fold and thrust belt, to Anatolia bounding the Arabian Plate from east to north. This blockage zone coincides well with the Arabian–Eurasian continent–continent collision, which is characterized by the uplift of the Zagros mountains and the Turkish–Iranian Plateau. The thick sedimentary cover of the Mesopotamian

Foredeep (or Zagros Foreland) and the reported crustal root beneath the Zagros (Snyder & Barazangi 1986) are typical crustal attenuating environments for  $Lg$  paths across the Zagros. We observed an approximate offset of 100 to 200 km in the location of minimum  $Lg/Pg$  differential attenuation in comparison to the location of the crustal root. The shift could be due to a lack of stations in the Zagros making the east–west ray paths dominant and smearing the blockage zone westward in the model.  $Lg$  propagation in the Turkish–Iranian Plateau is mostly blocked or attenuated, which could be due to the intrinsic attenuation in the crustal waveguide caused by partial melts in this region. This inference is supported by the widespread young volcanism in the region. Finally, the observed  $Lg$  blockage in the Mediterranean is consistent with the oceanic nature of most of the region.

The  $Lg$  phase was more efficient in the Arabian Shield than in the Arabian Platform. The shield (dark blue) mapped in our  $Lg/Pg$  model matches extremely well the basement map of Fig. 1. In general, the Arabian Plate in our tomographic  $Lg/Pg$  model is mainly an

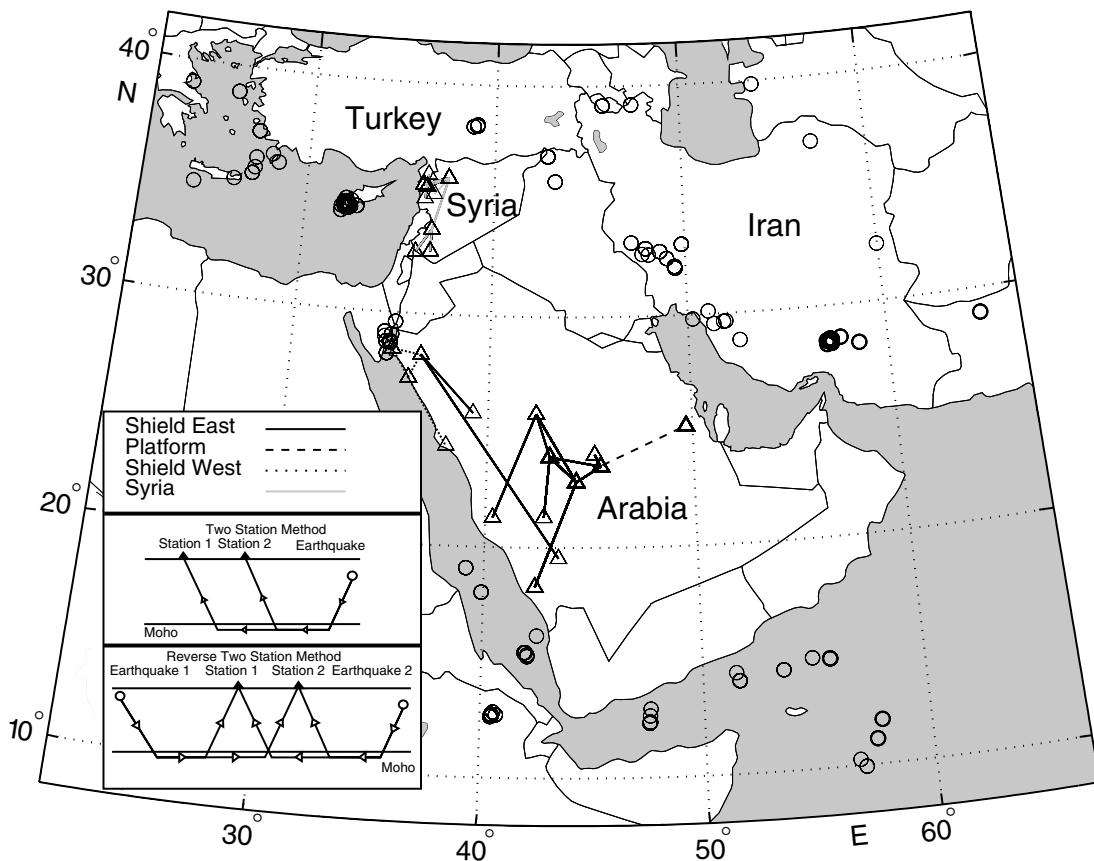


**Figure 13.** Map showing all the earthquake (circles) and station (triangles) combinations used to estimate  $Q_{Pn}$  (attenuation factor).  $Q_{Pn}$  have been estimated along the lines connecting stations. In the inset, schematic cartoons show the reverse two stations method and the two stations method used to estimate  $Q_{Pn}$ .

efficient region; the fading of the  $Lg/Pg$  ratio in the platform could be associated with the thick sedimentary cover of the platform becoming attenuating for  $Lg$ . Our limited observations in Oman show inefficient  $Lg$  propagation, which could be associated with a change in crustal thickness, for example the existence of a crustal root under the Oman mountains (Al-Lazki *et al.* 2002). The  $Lg$  blockage in the Gulf of Oman can be attributed to the existence of oceanic crust up to the entrance of the Arabian/Persian Gulf. This result is consistent with the entire Gulf of Oman consisting of oceanic crust.

$Lg$  blockage in oceanic or very thin continental crust has been documented in several studies (e.g. Press & Ewing 1952; Searle 1975; Zhang & Lay 1995; Sandvol *et al.* 2001). Along the Red Sea we observed some lateral variation in the  $Lg/Pg$  ratio tomography indicating a possible change in crustal characteristics. In the northern part of the Red Sea along the Egyptian coastline, a zone of  $Lg$  blockage was observed in agreement with crustal studies indicating the presence of oceanic crust along the Red Sea coast (Makris & Rhim 1991). The second main area of  $Lg$  blockage extends from about latitude  $17^\circ$  south to the southern end of the Red Sea and across to the Afar Depression. This region is mainly centred on Danakil Island and the Danakil Depression and extends to Afar. The existence of oceanic crust between  $15.9^\circ$  and  $26^\circ$  along the Red Sea axis has been confirmed by magnetic profiles analysed by Chu & Gordon (1998). Also, Afar is a region of thinned crust (Sandvol *et al.* 1998) and active volcanics. The crust in this whole region could be either thin (oceanic) or thinned continental crust due to the process of stretching and the opening of the Red Sea. An important

new result is that  $Lg$  efficiently propagate across the central sector of the Red Sea. This suggests major lateral variations in the crust along the Red Sea. The  $Lg$  blockage zone in Afar continues to the east along the Gulf of Aden down to the Owen fracture zone, where seismic and magnetic studies of this region found an oceanic crust with an age of about 10 Ma (Cochran 1981).

$Sn$  attenuation is more susceptible to anomalous change in temperature and/or partial melts in the upper mantle. In our tomographic  $Sn$  model (Fig. 8b) we observed a major  $Sn$  blockage zone in the Turkish–Iranian Plateau and along and to the east of the Dead Sea fault system. Low  $Pn$  velocities were observed in central and eastern Turkey as well as the Caucasus and east of the DSFS (Hearn & Ni 1994; Al-Lazki *et al.* 2003).  $Sn$  blockage coupled with low  $Pn$  velocities points to the existence of partial melt in the uppermost mantle (i.e. the mantle lid) of the Anatolian Plateau as a possible source of blockage and attenuation. To some degree this is substantiated by the existence of widespread Neogene/Quaternary volcanics and active volcanoes (see Fig. 16). We observed  $Sn$  blockage in the Iranian Plateau; however, our observations consist predominantly of relatively long propagation paths which limits our resolution of the extent of  $Sn$  attenuation. On the other hand, low  $Pn$  velocities observed in the region (Hearn & Ni 1994; Al-Lazki *et al.* 2003), coupled with high  $Sn$  attenuation, could indicate an anomalously hot lithosphere. The presence of anomalously attenuating and slow uppermost mantle beneath most of the Turkish–Iranian Plateau is consistent with localized mantle upwelling caused by the detachment of the subducted Neo-Tethys slab during the late Miocene. A large zone of  $Sn$  blockage extending from the eastern Mediterranean

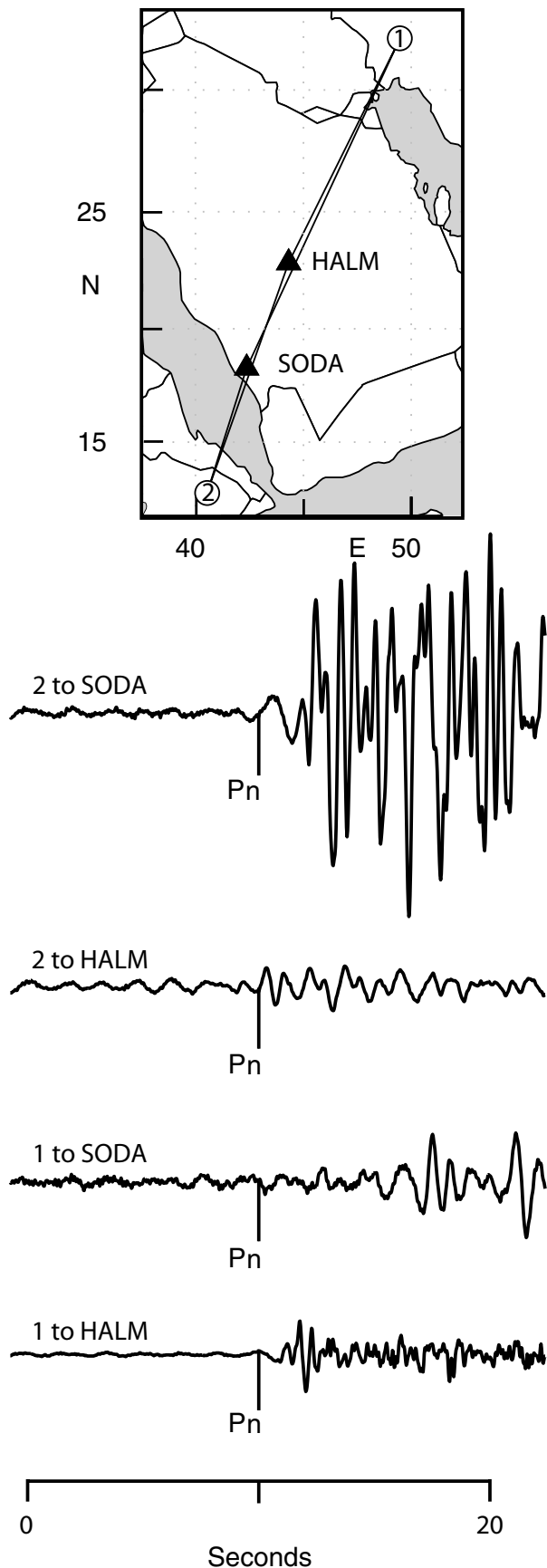


Figure 14. Sample seismograms (vertical component) used to estimate  $Q_{Pn}$  for the eastern part of the Arabian Shield (see inset map for location).

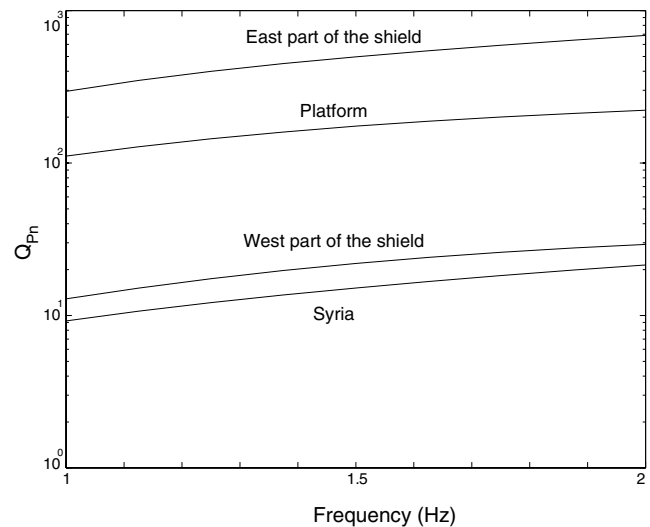


Figure 15. Plot showing  $Q_{Pn}$  estimate versus frequency for the western Arabian Shield, the eastern Arabian Shield, the Arabian Platform and in Syria.

coast to Jordan, Syria and northwestern Iraq was imaged. The region is characterized by widespread Neogene/Quaternary volcanics as well as very low  $Pn$  velocities (Fig. 16) (Hearn & Ni 1994; Al-Lazki *et al.* 2003) and very low  $Q_{Pn}$  (Fig. 15).

We also observed a region of extensive  $Sn$  blockage along the eastern edge of the Dead Sea fault system (DSFS) and farther to the east beneath most of Syria and Jordan (Fig. 8b). We argue for a possible absence of the lithospheric mantle in this region where the asthenosphere could be in direct contact with the lower crust. This regional anomaly cannot be attributed to continental rifting, since with the exception of the localized pull-apart basins, the DSFS is primarily a transform plate boundary with little, if any, extension (e.g. McClusky *et al.* 2003; Joffe & Garfunkel 1987). The scale of the pull-apart basins is not significant enough to produce such an anomaly. Instead this high attenuation and low  $Pn$  velocities may be connected with the hot uppermost mantle from the Gulf of Aqaba, the Red Sea, the Afar triangle and East Africa (e.g. Daradich *et al.* 2003). We observed evidence that these lithospheric mantle anomalies may all be connected given the similar nature of their seismic signal and the geochemistry of the basaltic rocks (e.g. Camp & Roobol 1992). We suggest that the DSFS is not responsible for this outstanding major uppermost mantle anomaly, and that this anomaly may pre-date the development of the DSFS. In fact, it is possible that the location of the DSFS is a result of this upper mantle anomaly.

In most of the Arabian Platform, the Zagros, Makran and the Gulf of Oman we observed efficient  $Sn$ .  $Sn$  is more attenuated in the Arabian Shield than in the Arabian Platform, specifically in regions of Neogene/Quaternary volcanics, in Yemen and along the Red Sea coastal lines. Based on our observations we infer that the lithosphere is not hot or thinned across the entire Arabian Shield. The efficient  $Sn$  propagation zone in the Arabian Platform extends eastward to Zagros, where a clear change to inefficient or blocked  $Sn$  occurs along the suture or the thrust line.

A region of efficient  $Sn$  propagation in the central Red Sea is observed. This is a new and important result. In the northern part of the Red Sea (north of latitude  $22^\circ$ ) and along both the Gulf of Aqaba and the Gulf of Suez,  $Sn$  propagation is inefficient or blocked. These regions of efficient  $Sn$  and blockage indicate that the early stages of opening and seafloor spreading are not simple and uniform along

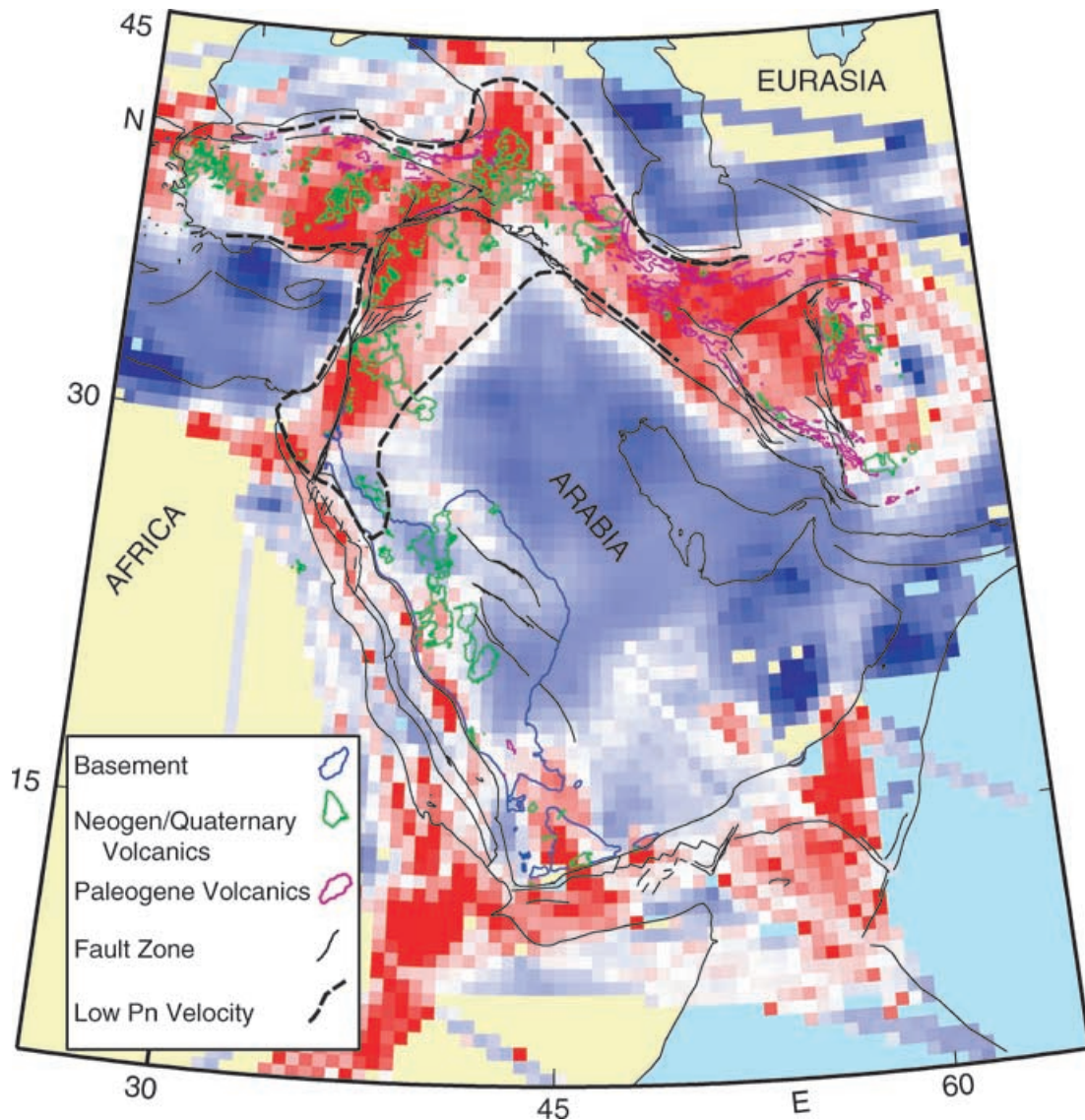


**Figure 16.** Map showing the  $S_n$  tomographic model overlain by the tectonic map of the region and the  $P_n$  contour lines corresponding to low  $P_n$  velocity (Al-Lazki *et al.* 2003). Regions of high  $S_n$  attenuation correlate well with regions of low  $P_n$  velocities. Also, regions of  $S_n$  attenuation correlates with regions of Cenozoic volcanics. See Fig. 8(b) for explanation of the colour-coded bar for  $S_n$  efficiency.

the Red Sea. In general along the Red Sea, regions of inefficient  $S_n$  propagation correlate well with regions of inefficient  $L_g$  propagation. A region of  $S_n$  attenuation in Afar extending north along the Danakil Depression, east along the Gulf of Aden and southwest along the East African rift has been clearly mapped by our  $S_n$  tomography model that is consistent with the presence of active volcanism and continental rifting.

#### ACKNOWLEDGMENTS

The authors would like to thank King Abdulaziz City for Science and Technology (KACST) for providing us with the digital recordings of the Saudi National Seismic Network and providing a scholarship for the first author. We would also like to thank Waris Warsi, Khalfan Al-Tobi and Salam Al-Hashmi of Sultan Qaboos University for their help in acquiring the Oman temporary network data. We are also grateful to A. Calvert for his help in MATLAB, C. Sandvol, S. Gallow, C. Brindisi, D. Seber, F. Gomez and G. Brew for their help in GIS, computer questions and helpful comments. We also thank

R. Mellors for a careful review of this manuscript. This research is partially supported by the National Science Foundation (Grant No EAR-9804780).

#### SUPPLEMENTARY MATERIAL

Figs S1–S6 are available online from <http://www.blackwell-publishing.com/products/journals/suppmat/GJI/GJI2246/GJI2246sm.htm>

#### REFERENCES

- Al-Lazki, A.I., Seber, D., Sandvol, E. & Barazangi, M., 2002. A crustal transect across the Oman mountains of the eastern margin of Arabia, *GeoArabia*, **7**, 47–78.
- Al-Lazki, A.I., Sandvol, E., Seber, D., Barazangi, M., Turkelli, N. & Mohamad, R., 2003.  $P_n$  tomographic imaging of mantle lid velocity and anisotropy at the junction of the Arabian, Eurasian, and African plates, submitted to, *Geophys. J. Int.*, submitted.

- Badri, M. & Sinno, Y., 1991. Qp crustal structure in central Saudi Arabia, *J. African Earth Sci.*, **12**, 561–568.
- Barka, A. & Reilinger, R., 1997. Active tectonics of the eastern Mediterranean region: deduced from GPS, neotectonic and seismicity data, *Ann. Geofis.*, **40**, 587–610.
- Baumgardt, D.R., 1996. Investigations of Lg blockage and transportability of regional discriminations in the Middle East, *Scientific Report 1*, PL-TR-96-2294, ENSCO Inc., Springfield, VA.
- Baumgardt, D.R. & Der, Z., 1997. Investigation of the transportability of the P/S ratio discriminate to different tectonic regions, *Scientific Report 1*, PL-TR-94-229, ENSCO, Inc., Springfield, VA.
- Bostock, M. & Kennett, B.L.N., 1990. The effect of 3-D structure on Lg propagation patterns, *Geophys. J. Int.*, **101**, 355–365.
- Bouchon, M., 1982. Complete synthesis of seismic crustal phases at regional distances, *J. geophys. Res.*, **87**, 1735–1741.
- Brew, G., Barazangi, M., Al-Maleh, A.K. & Sawaf, T., 2001. Tectonic and geologic evolution of Syria, *GeoArabia*, **6**, 573–616.
- Calvert, A., Sandvol, E., Seber, D., Barazangi, M., Vidal, F., Alguacil, G. & Jabour, N., 2000. Propagation of regional seismic phases (Lg and Sn) and Pn velocity structure along the Africa-Iberia plate boundary zone: tectonic implications, *Geophys. J. Int.*, **142**, 384–408.
- Camp, V.E. & Roobol, M.J., 1992. Upwelling asthenosphere beneath western Arabia and its regional implications, *J. geophys. Res.*, **97**, 15 255–15 271.
- Chu, D. & Gordon, R., 1998. Current plate motion across the Red Sea, *Geophys. J. Int.*, **135**, 313–328.
- Chun, K.Y., 1986. One-parameter approach to surface wave  $\gamma$  measurement, *Earthquake Notes*, **57**, 4, 111.
- Chun, K.Y., West, G.F., Kokoski, R.J. & Samson, C., 1987. A novel technique for measuring Lg attenuation: results from eastern Canada between 1 to 10 Hz, *Bull. seism. Soc. Am.*, **77**, 398–419.
- Cochran, J.R., 1981. The Gulf of Aden, structure and evolution of a young ocean basin and continental basin, *J. geophys. Res.*, **86**, 263–288.
- Cochran, J.R., 1983. Model for development of the Red Sea, *Am. Assoc. Petrol. Geol. Bull.*, **67**, 41–69.
- Cochran, J.R. & Martinez, F., 1988. Structure and tectonics of the northern Red Sea: catching a continental margin between rifting and drifting, *Tectonophysics*, **150**, 1–32.
- Cong, L. & Mitchell, B., 1998. Lg coda Q and its relation to the geology and tectonics of the Middle East, *Pure appl. Geophys.*, **153**, 563–585.
- Cong, L.L., Xie, J.K. & Mitchell, B., 1996. Excitation and propagation of Lg from earthquakes in Central Asia with implications for explosion/earthquake discrimination, *J. geophys. Res.*, **101**, 27 779–27 789.
- Daradich, A., Mitrovica, J.X., Pysklywec, R.N., Willett, S.D. & Forte, A.M., 2003. Mantle flow, dynamic topography, and rift-flank uplift of Arabia, *Geology*, **31**, 901–904.
- Dewey, J.F. & Sengor, A., 1979. Aegean and surrounding regions: complex multiplate and continuum tectonics in a convergence zone, *Geol. Soc. Am. Bull.*, **90**, 84–92.
- Dewey, J.F., Pitman, W., Ryan, W. & Bonnin, J., 1973. Plate tectonics and the evolution of the Alpine system, *Geol. Soc. Am. Bull.*, **84**, 3137–3180.
- Fan, G. & Lay, T., 1998. Statistical analysis of irregular waveguide influences on regional seismic discriminates in China, *Bull. seism. Soc. Am.*, **88**, 74–88.
- Farhoudi, G. & Karig, D., 1977. Makran of Iran and Pakistan as an active arc system, *Geology*, **5**, 664–668.
- Garfunkel, Z., 1981. Internal structure of the Dead Sea leaky transform (rift) in relation to plate kinematics, *Tectonophysics*, **80**, 81–108.
- Gok, R., Turkelli, N., Sandvol, E., Seber, D. & Barazangi, M., 2000. Regional wave propagation in Turkey and surrounding regions, *Geophys. Res. Lett.*, **27**, 429–432.
- Hartse, H., Flores, R. & Johnson, P., 1998. Correcting regional seismic discriminants for path effect in western China, *Bull. seism. Soc. Am.*, **88**, 596–608.
- Hearn, T.M. & Ni, J.F., 1994. Pn velocity beneath continental collision zones: the Turkish-Iranian Plateau, *Geophys. J. Int.*, **117**, 273–283.
- Hempton, M., 1987. Constraints on Arabian plate motion and extensional history of the Red Sea, *Tectonics*, **6**, (2), 687–705.
- Hill, D.P., 1973. Critically refracted waves in a spherically symmetric radially heterogeneous earth model, *Geophys. J. R. astr. Soc.*, **46**, 407–432.
- Huestis, S., Molnar, P. & Oliver, J., 1973. Regional Sn velocities and shear velocity in the uppermost mantle, *Bull. seism. Soc. Am.*, **63**, 469.
- Jacob, K. & Quittmeyer, R., 1979. The Makran region of Pakistan and Iran: trench-arc system with active plate subduction, in *Geodynamics of Pakistan*, pp. 305–317, eds Farah, A. & DeJong, K., Geological Survey of Pakistan, Quetta.
- Joffe, S. & Garfunkel, Z., 1987. Plate kinematics of the circum Red Sea; a re-evaluation, *Tectonophysics*, **141**, 5–22.
- Kadinsky-Cade, K. & Barazangi, M., 1982. Seismotectonics of southern Iran: The Oman line, *Tectonics*, **1**, 389–412.
- Kadinsky-Cade, K., Barazangi, M., Oliver, J. & Isacks, B., 1981. Lateral variation in high frequency seismic wave propagation at regional distances across the Turkish and Iranian plateaus, *J. geophys. Res.*, **86**, 9377–9396.
- Kennett, B.L.N., 1986. Lg waves and structural boundaries, *Bull. seism. Soc. Am.*, **76**, 1133–1141.
- Le Pichon, X. & Girdler, J.M., 1988. The rotation of Arabia and the Levant fault system, *Tectonophysics*, **153**, 271–294.
- Makris, M.J. & Rhim, R., 1991. Shear-controlled evolution of the Red Sea: pull-apart model, *Tectonophysics*, **198**, 441–446.
- McClusky, S., Reilinger, R., Mahmoud, S., Sari, D.B. & Tealeb, A., 2003. GPS constraints on Africa (Nubia) and Arabian plate motion, *Geophys. J. Int.*, **155**, 126–138.
- McKenzie, D., 1976. The East Anatolian fault; a major structure in eastern Turkey, *Earth planet. Sci. Lett.*, **29**, 189–193.
- McKenzie, D.P., Davies, D. & Molnar, P., 1970. Plate tectonics of the Red Sea and East Africa, *Nature*, **226**, 242–248.
- Mellors, R., Vernon, F., Camp, V., Al-Amri, A., Ghalib, A. & Al-Dail, M., 1999. Regional wave propagation in the Saudi Arabian peninsula, *Geophys. Res. Lett.*, **104**, 20 221–20 235.
- Mitchell, B.J., Pan, Y., Xie, J. & Cong, L., 1997. Lg coda Q variation across Eurasia and its relation to crustal evolution, *J. geophys. Res.*, **102**, 22 767–22 779.
- Mokhtar, T.A., Ammon, C.A., Herrmann, R.B. & Ghalib, A.A., 2001. Surface wave velocity across Arabia, *Pure appl. Geophys.*, **158**, 1425–1444.
- Molnar, P. & Oliver, J., 1969. Lateral variation of attenuation in the uppermost mantle and discontinuities in the lithosphere, *J. geophys. Res.*, **74**, 2648–2683.
- Nuttli, O., 1980. The excitation and attenuation of seismic crustal phases in Iran, *Bull. seism. Soc. Am.*, **70**, 469–480.
- Paige, C.C. & Saunders, M.A., 1982. LSQR: An algorithm for sparse linear equations and sparse least squares, *ACM Trans. Math. Software*, **8**, 43–71.
- Park, J., 1987. Multitaper spectral analysis of high-frequency seismograms, *J. geophys. Res.*, **92**, 12 675–12 684.
- Phillip, H., Cisternas, A., Gvishiani, A. & Gorshkov, A., 1989. The Caucasus: an actual example of the initial stages of continental collision, *Tectonophysics*, **161**, 393–398.
- Phillips, W.S., Hartse, H.E., Taylor, S., Velasco, A.A. & Randall, G.E., 2001. Application of regional phase amplitude tomography to seismic verification, *Pure appl. Geophys.*, **158**, 1189–1206.
- Powers, R.W., Ramirez, L.F., Redmond, C.P. & Elberg, E.L., 1966. *Geology of the Arabian Peninsula: Sedimentary Geology of Saudi Arabia*, US Geological Survey Professional Paper 560-D, pp. 91–96.
- Press, F. & Ewing, M., 1952. Two slow surface waves across North America, *Bull. seism. Soc. Am.*, **42**, 219–228.
- Rodgers, A., Ni, J. & Hearn, T., 1997. Propagation characteristics of short-period Sn and Lg in the Middle east, *Bull. seism. Soc. Am.*, **87**, 396–413.
- Sandvol, E., Al-Damegh, K., Calvert, A., Seber, D., Barazangi, M., Mohamad, R., Gok, R., Turkelli, N. & Gurbuz, C., 2001. Tomographic imaging of observed regional wave propagation in the Middle East, *Pure appl. Geophys.*, **158**, 1121–1163.
- Sandvol, E., Seber, D., Barazangi, M., Vernon, F., Mellors, R. & Al-Amri, A., 1998. Lithospheric seismic velocity discontinuities beneath the Arabian shield, *Geophys. Res. Lett.*, **25**, (15), 287–2876.
- Searle, R.C., 1975. The dispersion of surface waves across the Afar, in *Afar Depression of Ethiopia*, pp. 113–120, eds Pilgerand, A. & Roesler, A., Schweizerbart, Stuttgart, Germany.

- Seber, D., Vallve, M., Sandvol, E., Steer, D. & Barazangi, M., 1997. Middle East tectonics: applications of geographic information system (GIS), *GSA Today*, **7**, 1–6.
- Sengor, A.M.C. & Kidd, W.S.F., 1979. Post-collisional tectonics of the Turkish-Iranian Plateau and a comparison with Tibet, *Tectonophysics*, **55**, 361–376.
- Sereno, T.J., 1989. Numerical modeling of Pn geometric spreading and empirically determination attenuation of Pn and Lg phases recorded in eastern Kazakhstan, *Technical Report of Science Application International Corporation, SAIC 89/1555*, San Diego, CA.
- Snyder, D. & Barazangi, M., 1986. Deep crustal structure and flexure of the Arabian plate beneath the Zagros collisional mountain belt as inferred from gravity observations, *Tectonics*, **5**, 361–373.
- Stocklin, J., 1974. Possible ancient continental margins in Iran, in, *Geology of Continental Margins*, pp. 873–877, eds Burk, C. & Drake, C., Springer-Verlag, New York.
- Zhang, T.R. & Lay, T., 1995. Why the Lg phase does not traverse oceanic crust, *Bull. seism. Soc. Am.*, **85**, 1665–1678.
- Zhu, T., Chun, K. & West, G.F., 1991. Geometrical spreading and Q of Pn waves: an investigative study in eastern Canada, *Bull. seism. Soc. Am.*, **81**, 882–896.
- Zonenshain, L. & LePichon, X., 1986. Deep basins of the Black Sea and Caspian Sea as remnants of Mesozoic back-arc basins, *Tectonophysics*, **123**, 181–211.